Cell

Mapping Local and Global Liquid Phase Behavior in Living Cells Using Photo-Oligomerizable Seeds

Graphical Abstract

Highlights

- Corelets are phase-separating photoinduced oligomers of self-interacting proteins

- FUS$_N$ Corelets phase diagram with binodal and spinodal regimes mapped in live cells

- Mutations reshape phase diagrams allowing quantitative sequence space interrogation

- Localized oligomerization drives condensation even at undersaturated concentrations

Authors

Dan Bracha, Mackenzie T. Walls,
Ming-Tzo Wei, ..., José L. Avalos,
Jared E. Toettcher,
Clifford P. Brangwynne

Correspondence

cbrangwy@princeton.edu

In Brief

Probing cellular phase separation with a biomimetic system suggests a mechanism for condensate formation with low abundance molecules.
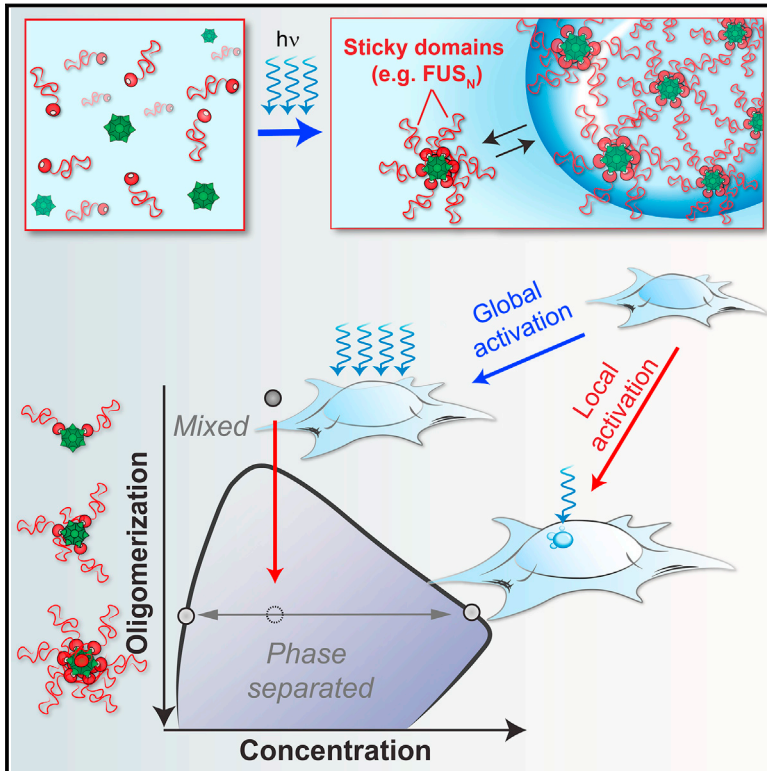
CellPress

Article

Mapping Local and Global Liquid Phase Behavior in Living Cells Using Photo-Oligomerizable Seeds

Dan Bracha,[1] Mackenzie T. Walls,[1] Ming-Tzo Wei,[1] Lian Zhu,[1] Martin Kurian,[1] José L. Avalos,[1,2] Jared E. Toettcher,[3] and Clifford P. Brangwynne[1,4,5,6,*]

[1]Department of Chemical and Biological Engineering, Princeton University, Princeton, NJ 08544, USA
[2]The Andlinger Center for Energy and the Environment, Princeton University, Princeton, NJ 08544, USA
[3]Department of Molecular Biology, Princeton University, Princeton, NJ 08544, USA
[4]Lewis Sigler Institute for Integrative Genomics, Princeton University, Princeton, NJ 08544, USA
[5]Howard Hughes Medical Institute, Princeton University, Princeton, NJ 08544, USA
[6]Lead Contact
*Correspondence: cbrangwy@princeton.edu
https://doi.org/10.1016/j.cell.2018.10.048

SUMMARY

Liquid-liquid phase separation plays a key role in the assembly of diverse intracellular structures. However, the biophysical principles by which phase separation can be precisely localized within subregions of the cell are still largely unclear, particularly for low-abundance proteins. Here, we introduce an oligomerizing biomimetic system, "Corelets," and utilize its rapid and quantitative light-controlled tunability to map full intracellular phase diagrams, which dictate the concentrations at which phase separation occurs and the transition mechanism, in a protein sequence dependent manner. Surprisingly, both experiments and simulations show that while intracellular concentrations may be insufficient for global phase separation, sequestering protein ligands to slowly diffusing nucleation centers can move the cell into a different region of the phase diagram, resulting in localized phase separation. This diffusive capture mechanism liberates the cell from the constraints of global protein abundance and is likely exploited to pattern condensates associated with diverse biological processes.

INTRODUCTION

Living cells have evolved strategies for organizing their contents by compartmentalizing specific sets of biomolecules into a variety of different organelles. In addition to the canonical vesicle-like organelles, there are dozens of different types of intracellular bodies that are not membrane-bound—from the nucleolus and stress granules to processing bodies and signaling clusters. These structures, referred to as membrane-less organelles or condensates, represent dynamic molecular assemblies, which can play numerous roles in living cells: sequestering biomolecules, facilitating reactions, and channeling intracellular signaling (Banani et al., 2017; Shin and Brangwynne, 2017).

Studies on intracellular condensates have revealed that their assembly arises from liquid-liquid phase separation driven by weak multivalent interactions often involving intrinsically disordered protein regions (IDPs/IDRs) and nucleic acids (Brangwynne et al., 2009, 2011; Elbaum-Garfinkle et al., 2015; Li et al., 2012; Nott et al., 2015). These interactions give rise to stable condensed forms of biomolecular organization, which typically exhibit dynamic molecular exchange and liquid phase fluidity.

In many cases, these condensates are spatially patterned within living cells, as seen with germline P granules, which form via liquid-liquid phase separation that is modulated across the anterior-posterior embryo axis, giving rise to an asymmetric localization implicated in early cell fate specification (Brangwynne et al., 2009; Smith et al., 2016). The nucleolus is a particularly notable example of a phase separated body formed at specific genomic loci (Berry et al., 2015; Feric et al., 2016; Zhu and Brangwynne, 2015). Moreover, it has become apparent that many nuclear condensates are likewise present at transcriptionally active genes (Cho et al., 2018; Chong et al., 2018; Sabari et al., 2018), while HP1a/α proteins conversely appear to drive phase separation at regions of transcriptionally inactive heterochromatin (Larson et al., 2017; Strom et al., 2017). RNA accumulation (Berry et al., 2015), chemical reactivity (Zwicker et al., 2014), and morphogen gradients (Brangwynne et al., 2009) have been proposed to drive patterned phase separation. Nevertheless, it is still unclear how IDPs and other interacting ligands distributed throughout the cell, often at relatively dilute concentrations, can be rapidly and precisely induced to condense at particular subcellular locations.

In condensed matter physics and material science, phase diagrams are mapped through experiment and understood through rigorous theory. These graphical representations quantitatively define the system parameters associated with different states of matter, which reflect minimization of the thermodynamic free energy of the system. Non-living systems often exhibit a binodal curve that circumscribes the parameters that give rise to phase separation and dictates the concentrations of the phases formed (Dill and Bromberg, 2011; Rubinstein and Colby, 2003). Work toward understanding the phase behavior of biomolecules *in vitro* has shown that proteins can also exhibit
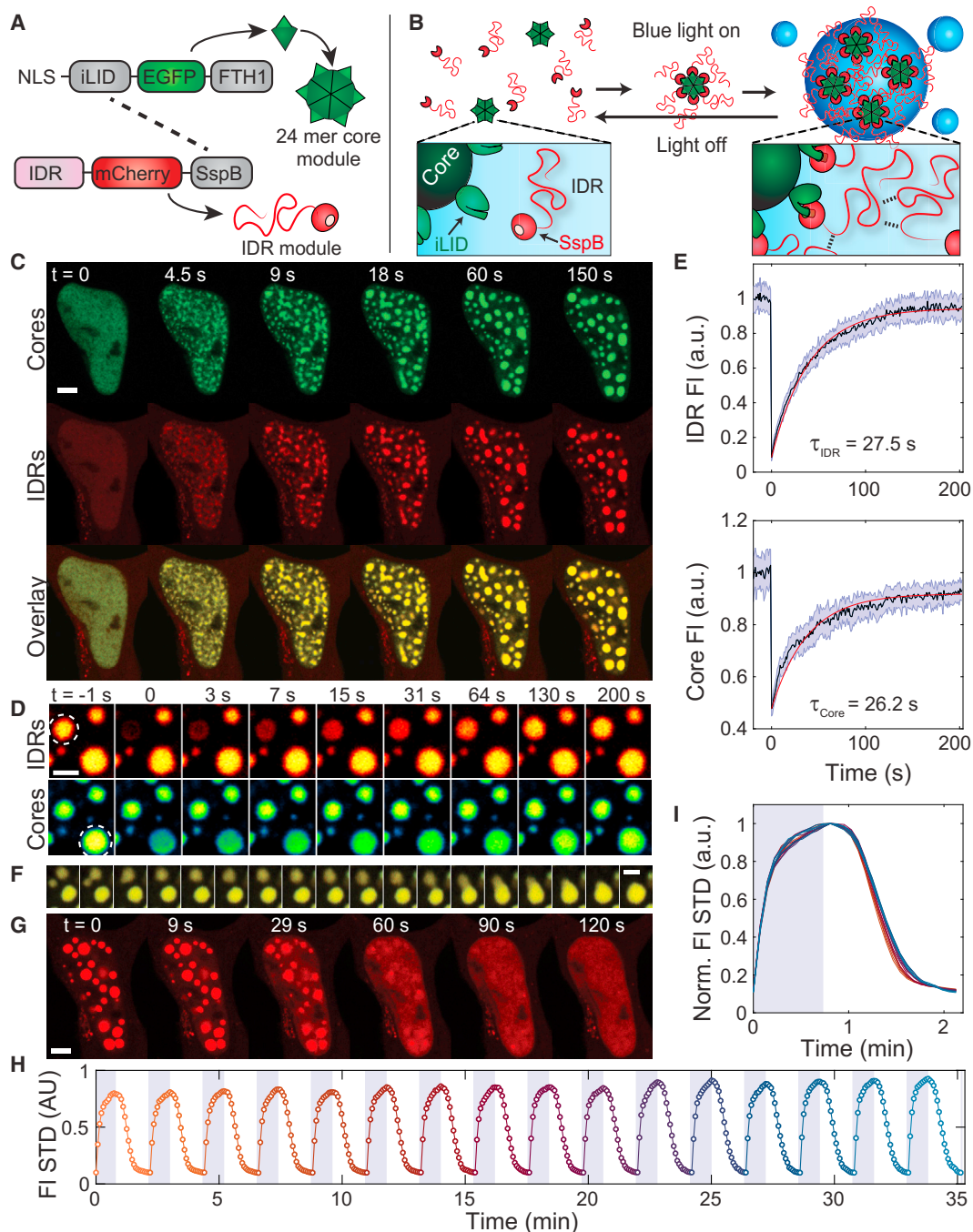
Figure 1. Corelets Enable Light-Activated Intracellular Droplet Condensation

(A) Schematic diagram of the Corelet system. Corelets consists of two modules: first, a nuclear targeted, GFP-tagged ferritin core functionalized by 24 photo-activatable iLID domains; and second, iLID's cognate partner, SspB, mCherry-tagged and conjugated to a self-interacting protein domain, such as the N-terminal IDR of FUS. Dashed line designate photo-inducible heterodimerizing units.

(B) Schematic of Corelet phase separation. Upon global blue-light illumination, up to 24 IDR modules are captured by each Core, which may subsequently phase separate by multivalent IDR interactions in a reversible manner.

(C) Time lapse confocal imaging of photo-activated FUS_N Corelet-expressing HEK293 cells (also shown in Video S1 for multiple cells). Images show phase separation with colocalization of Cores (green) and FUS_N IDRs (red). See also Figure S1 for IDR-free controls and Figure S2 for recruitment through IDR rather than SspB.

(D) FUS_N Corelet condensates exhibit liquid-like properties as inferred by rapid fluorescence recovery after photo-bleaching of both FUS_N IDR (top) and Core components (bottom), shown as heat colormaps of the florescence. FRAP region of interest (ROI) labeled with dashed circles.

(legend continued on next page)

quantifiable binodal phase boundaries (Asherie, 2004; Broide et al., 1991; Wei et al., 2017). However, understanding biomolecular phase behavior in living cells with such precision has been challenging, due to the lack of tools for triggering, shaping, or destabilizing condensates in the cellular environment. As a result, the proposal that these equilibrium thermodynamic concepts can be quantitatively applied in living cells remains in question.

Recently, we developed a photo-activated system for reversibly controlling IDR-driven phase transitions using photo-oligomerizable CRY2 proteins, termed "optoDroplets" (Shin et al., 2017). This system showed a threshold saturation concentration for phase separation, consistent with classic liquid-liquid phase separation, which was linked to a subsequent gelation transition. However, multiple characteristics of the CRY2 proteins inhibited the use of this system for rigorous quantification of its resulting phase behavior. In particular, CRY2 forms poorly characterized polydisperse oligomers yielding an undefined ensemble of multivalent particles. CRY2 deactivation time is several minutes, precluding tight local activation due to diffusion of molecules away from the activation zone (Shin et al., 2017). Moreover, CRY2 homotypic interactions may be directly involved in the network of interactions within the optoDroplet condensate, through continuous association and dissociation, and therefore may confound the contribution of the IDR to phase behavior. Another recent study formed intracellular hydrogels with light- and chemically activated multimerized interaction domains (Nakamura et al., 2018). To date, however, no tools have enabled quantitative mapping of intracellular phase diagrams, leaving the field with a highly descriptive and imprecise understanding of patterned phase separation and other non-equilibrium features inherent to phase separation in living cells.

To address this gap, we developed an optogenetic system inspired by endogenous molecular architectures, in which the effective oligomerization of IDR-rich proteins appears to be key for driving phase separation. For example, nascent rRNA transcripts (Berry et al., 2015; Falahati et al., 2016) or long non-coding RNA (lncRNA), such as NEAT1 (West et al., 2014), and other types of RNA are associated with specific DNA loci and may serve as scaffolds for locally enriching self-interacting IDPs (Dundr and Misteli, 2010); DNA itself could also serve as an oligomerization platform for promoting local transcriptional condensates (Cho et al., 2018; Chong et al., 2018; Sabari et al., 2018). Finally, a number of proteins appear to self-oligomerize to drive phase separation. For example, NPM1 pentamerizes to form a radial array of IDRs and RNA-binding domains necessary for phase separation and nucleolus assembly (Feric et al., 2016; Mitrea et al., 2016). *C. elegans* PGL proteins also contain a dimerization domain that is important for patterned P granule phase separation (Aoki et al., 2018). Stress granules present yet another example, where oligomerization of G3BP1/2 proteins is important for stress granule condensation (Tourrière et al., 2003). Inspired by these native molecular architectures, we reasoned that an approach to precisely control the oligomerization state of IDPs could elucidate the underlying biophysical mechanisms by which intracellular phase transitions are controlled in cells, both globally and locally.

RESULTS

Corelets Enable Light-Activated Intracellular Droplet Condensation

To parse the effect of multivalent scaffolding of IDRs on intracellular phase separation, we developed Corelets (*Core* scaffolds to promote drop*lets*): a two-module optogenetic system that mimics the native oligomerization of IDR-rich proteins, using a light-activatable high valency core. The core is comprised of 24 human ferritin heavy chain (FTH1) protein subunits, which self-assemble to form a spherical particle of 12 nm diameter (herein referred to as a "Core"). When functionalized by self-interacting modules, these particles can give rise to supramolecular clusters (Bellapadrona and Elbaum, 2014). We therefore fused FTH1 to a nuclear localization signal (NLS) and an engineered protein iLID, which strongly heterodimerizes (K_d ~130 nM) with its cognate partner, SspB, in response to blue light activation (Guntas et al., 2015) (Figure 1A). For the second module of the Corelet system, SspB was fused to various self-interacting IDRs, as well as full-length IDR-containing proteins, implicated as drivers of intracellular phase separation, such that the ferritin core would serve as a well-defined multivalent scaffold for light-activated IDR oligomerization (Figure 1A).

In response to blue light activation, as many as 24 IDRs are induced to directly assemble on each Core, thus rapidly forming self-interacting particles (Figure 1B). We first utilized an N-terminal FUS IDR (FUS_N) fused to SspB. For this FUS_N Corelet system, condensation is apparent within ~1–2 s after blue light illumination and reaches a steady state within a few minutes (Figure 1C; Video S1). These FUS_N Corelet condensates are liquids, as apparent from the rapid and nearly complete fluorescence recovery after photobleaching (FRAP) of both Core and IDR components (Figures 1D and 1E). This is further supported by the condensate's ability to rapidly fuse with one another and round up upon contact (Figure 1F). Consistent with IDR-driven phase separation, we observe no condensates in control constructs lacking IDRs, even for high concentrations that do phase separate with IDRs (Figure S1), and we find significant recruitment of SspB-free FUS_N proteins to FUS_N-Corelet condensates (Figure S2). Thus, light-activated SspB-iLID dimerization does not directly contribute to the cohesive interactions of the emergent

(E) Quantified FRAP curves from (D). Mean and SD of fluorescence in quantified ROI are shown scaled by the pre-photobleached intensity. Red curves are exponential fits used to determine time constant of recovery, τ, as given in each panel.

(F) Corelet condensates rapidly fuse and coarsen (4.4 s between frames).

(G) Condensates completely disassemble within ~0.5–2 min after blue-light removal.

(H) Change in SD of nuclear IDR fluorescence indicates full reversibility during 15 on-and off cycles. See also Figure S3.

(I) Overlay of data from (G), showing little change in condensation and dissociation dynamics over multiple cycles (see also Figure S3D and STAR Methods). The curves corresponding to each cycle are colored to match (H).

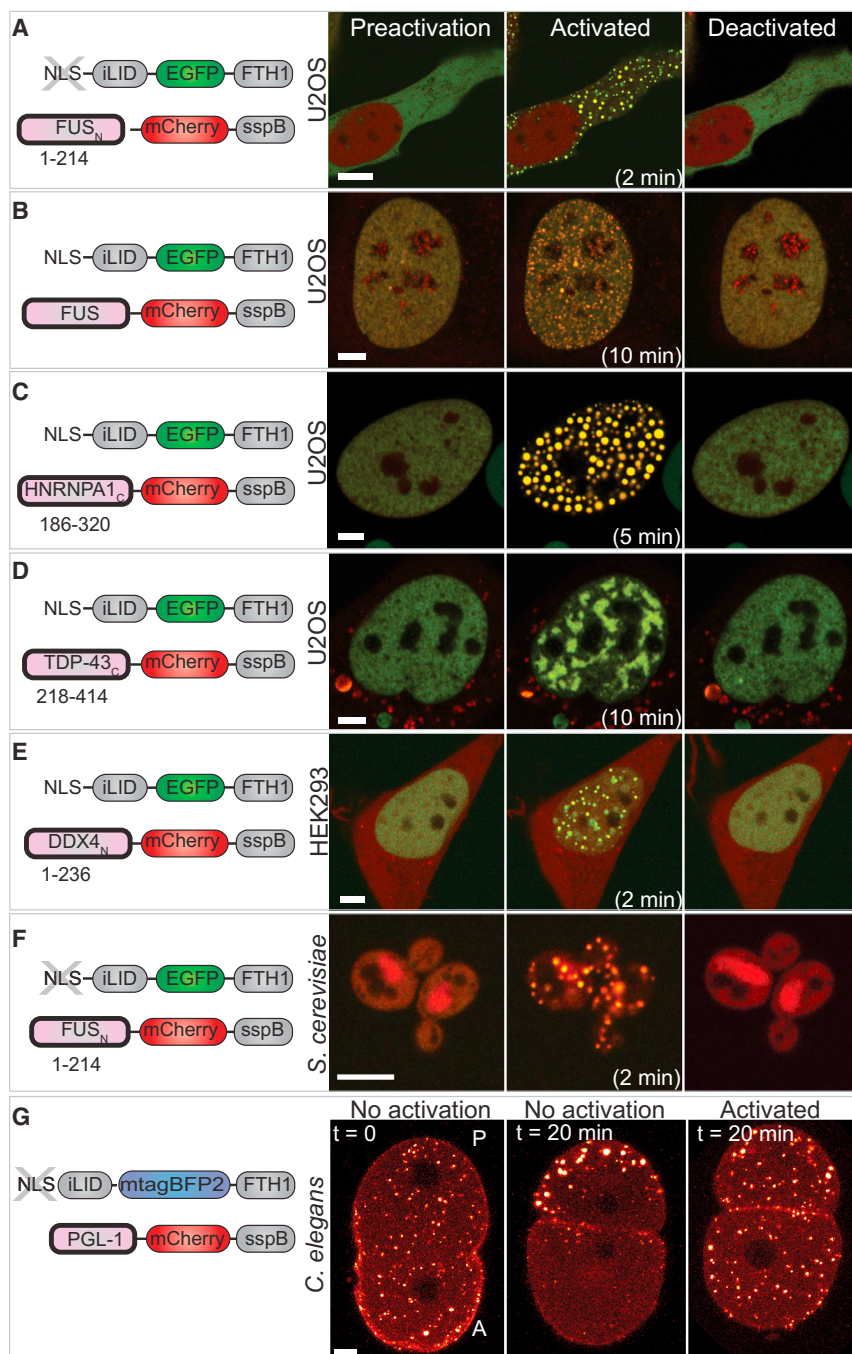Scale bars, 5 μm (C, G); 2 μm (D, F).

Figure 2. Corelets Drive Phase Separation with Different Self-Interacting IDRs and in Various Living Systems

(A–E) Fluorescence images of representative stable Corelet-expressing mammalian cultured cells utilizing various IDR/IDPs with nuclear or cytoplasmic Cores, resulting in light-sensitive, reversible condensates in all cases. Schematic of utilized constructs shown on the left corresponding to adjacent images. (A) Cytoplasmic FUS_N IDR Corelets (no NLS). (B) Full-length FUS Corelets. (C) $HNRNPA1_C$ Corelets. (D) $TDP\text{-}43_C$ Corelets. (E) $DDX4_N$ Corelets. (A)–(D) are U2OS cells, (E) is HEK293. Images are taken before and after 2–10 min activation as indicated in each panel and 5 min after deactivation. All images show overlay of GFP Cores and mCherry IDR/IDP.

(F) *S. cerevisiae* expressing cytoplasmic FUS_N Corelets. Images as in (A)–(G), except GFP overlay is not shown for deactivation.

(G) Local and global activation of cytoplasmic PGL-1 IDP Corelets in *C. elegans* one-cell embryo during the first cleavage. Images shown as heat colormap of mCherry signal. With no light activation, PGL-1-SspB components are recruited to native P granules, which are initially distributed uniformly throughout the embryo (t = 0), and then segregate to the embryo posterior (P) (t = 20 min). Instead, under global activation, PGL-1 Corelet puncta appear throughout the embryo. Scale bars, 5 μm.

Corelets Drive Phase Separation with Different Self-Interacting IDRs and in Various Living Systems

Liquid Corelet condensates can form not only in the nucleus, but also in the cytoplasm, by excluding the NLS from Core constructs (Figure 2A). Full-length FUS can also be utilized as the self-interacting domain fused to SspB (Figure 2B). Moreover, similar phase separated liquid condensates can also be formed from Corelets comprising a number of different self-interacting IDR-containing constructs. These include IDRs from other RNA binding proteins associated with stress granules, such as $HNRNPA1_C$ and $TDP\text{-}43_C$, as well as the germ granule component $DDX4_N$ (Figures 2C–2E). The Corelet system can be used to dynamically assemble light-sensitive condensates not only in various cultured cell lines including U2OS and HEK293 (Figures 2A–2D and 2E, respectively) but also in *Saccharomyces cerevisiae*, with cytoplasmic FUS_N Corelets (Figure 2F) and *Caenorhabditis elegans*, with a Corelets utilizing the germ granule IDP, PGL-1 (Figure 2G).

Mapping Global FUS_N Corelet Phase Diagrams and Distinct Phase Separation Modes

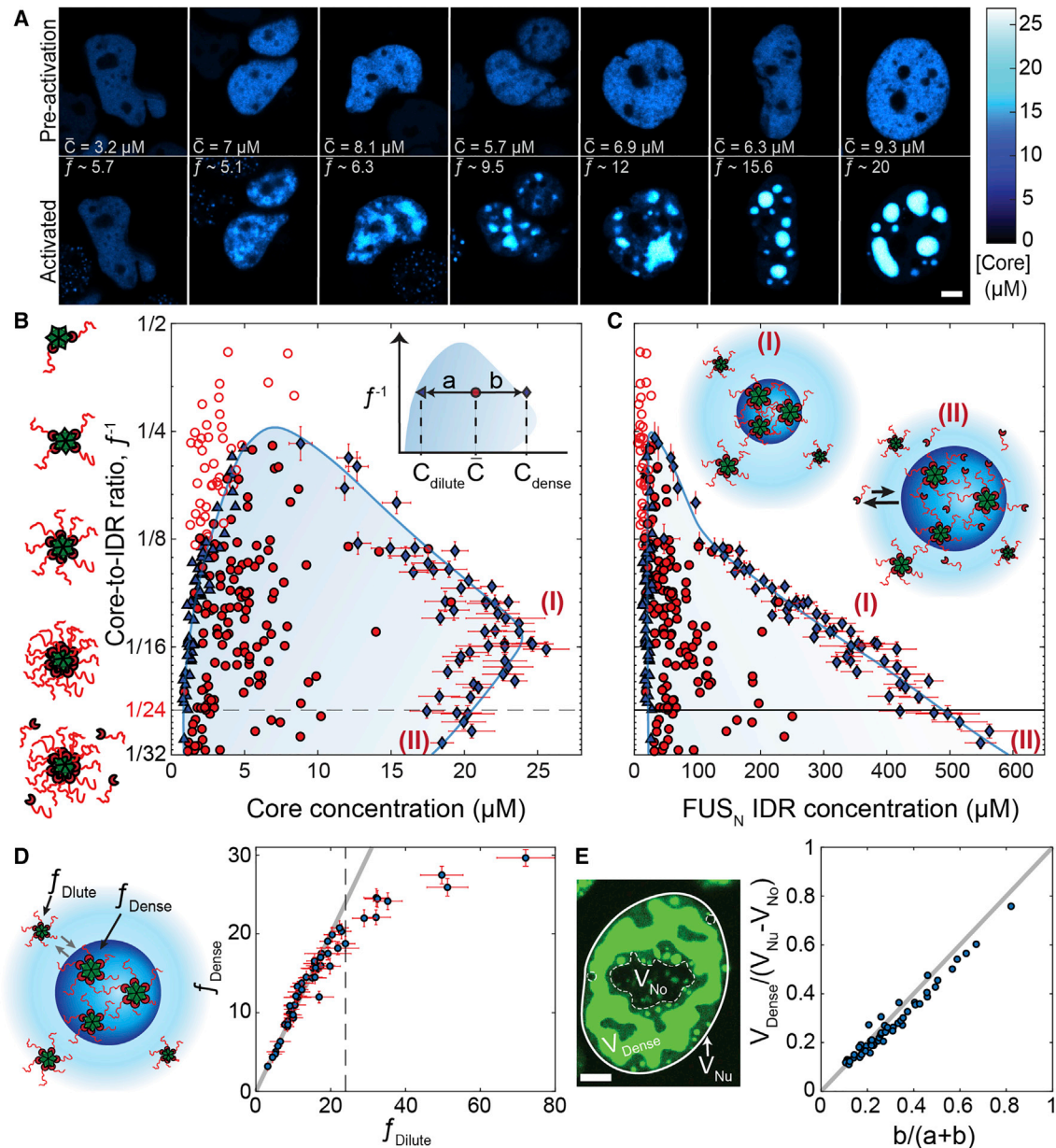The above findings suggest that Corelet activation may give rise to liquid-liquid phase separation. To quantitatively test this, we liquid phase, which instead rely on homotypic IDR-IDR interactions. Activation effectively gives rise to a one-component system of IDR-coated cores (Figures S3A–S3C). When activating illumination is turned off, the droplets quickly dissolve back to a uniform phase (Figure 1G). Moreover, when we applied sequences of uniform blue light activation cycles, FUS_N-Corelet condensates could be repetitively assembled through dozens of on-off cycles, with little apparent change in the disassembly kinetics (Figures 1H, 1I, and S3D).

Figure 3. Mapping Global FUS$_N$ Corelet Phase Diagrams

(A) Confocal images of Cores in FUS$_N$ Corelets expressing HEK293 cells with increasing average nuclear IDR-to-core ratio, $\bar{f}$, prior to activation (top) and after 10-min blue-light activation (bottom). Phase separation requires high enough Core concentration, and valency $\bar{f}$. Uniform fluorescence levels are observed throughout the dilute phase and within the various dense phases (see also Figures S4B–S4E). Color bar represents FCS-based fluorescence-to-concentration conversion (see Figure S4H and STAR Methods).

(B) Phase diagram of photo-activated FUS$_N$ Corelets, with respect to Core concentration and Core-to-IDR ratio, f^{-1}. Solid red circles indicate average nuclear concentrations for which phase separation is observed, while empty circles are concentrations where no phase separation is observed. Blue triangles and diamonds indicate concentrations of dilute phase and dense phase, respectively. Shaded two-phase region is bounded by approximated binodal curves drawn to align with measured dilute and dense phases and circumscribe phase separating average nuclear concentrations. Dashed horizontal line corresponds to fully coated Corelets with 24 IDRs per Core. Vertical axis on a $\log_2$ base. Inset: definition of lever rule parameters for measurement in (E). Note that a and b are defined with respect to the location of the measured dilute and dense phase points per cell, not the drawn binodal curve.

(C) Phase diagram of FUS$_N$ Corelets, with respect to IDR concentration. y axis and symbol definitions as in (B). Inset, schematic picture for species in the phase separated droplets for $f < 24$ (I) and $f > 24$ (II, saturated), showing recruitment of unbound IDRs into condensates of saturated Cores, which leads to an increase in IDR concentration in the dense phase but a decrease in Core concentration as a result of increased Core-to-Core spacing. These regions are similarly labeled with respect to dashed line in (B) and (C).

(legend continued on next page)

examined whether the observed transition exhibits quantitative signatures of liquid-liquid phase separation, well-known in non-living systems. We analyzed cells with different relative expression levels of the FUS_N-SspB and 24-mer NLS Ferritin-iLID components resulting from an unsorted population of virally infected cells. We define their average nuclear concentration ratio as $\bar{f} = \overline{[IDR]}/\overline{[Core]}$, which represents the mean number of IDRs-per-core upon activation ("valence," see Figure S4H and STAR Methods), as there is no observable expression of endogenous untagged Ferritin (Figure S4A). Calibrated pixel intensity histograms show a unimodal distribution of the core concentration before activation, while after activation phase separating cells exhibit broadened and even bimodal distributions (Figure S4B), with the two peaks representing two uniformly concentrated phases (Figures S4C–S4E) that become farther apart for cells with high $\bar{f}$ (Figure S4B). For cells with very low $\bar{f}$ and Core concentration, phase separation never occurs (Figure 3A, left panel $\bar{f} \sim 5.7$), while cells with higher $\bar{f}$ typically form distinct condensates with gradually increasing sphericity (Figure 3A, right panel $\bar{f} \sim 20$), consistent with $\bar{f}$ representing an effective interaction strength between IDR-decorated cores.

These data reflect the position of the cell with respect to a concave-down binodal phase boundary, as seen by plotting the inverse molar ratio $\bar{f}^{-1}$, against $\overline{[Core]}$ (Figures 3B and S4F–S4J). For a binodal phase boundary, the concentration of Cores measured outside of the droplets, $[Core]_{Dilute}$, demarcates the left-arm of the binodal. As expected for a phase-boundary, this curve accurately separates non-droplet forming cells and droplet-forming cells. The right arm of the binodal can be determined from the uniform protein concentration in droplets (Figures S4D and S4E) (Wei et al., 2017), in this case $[Core]_{Dense}$. At high $\bar{f}$, this concentration corresponds to a mean center-to-center spacing between Cores of ~ 40 nm, with Corelet components occupying $\sim 5\%$ of the condensate volume (see STAR Methods). Our determination of the location of the binodal is further supported by the lever rule for the volume fraction of droplets (Figures 3E and S4F). Moreover, cells near the peak of the phase diagram exhibit condensates with irregular morphology and undulating boundaries (Figure 3A, second and third panel), as expected for vanishing surface tension in the vicinity of a critical point (Honerkamp-Smith et al., 2009).

The molar ratio inside droplets, f_{Dense}, and outside droplets, f_{Dilute}, are typically very close, and similar to $\bar{f}$ (Figure 3D, $f_{Dilute} < 24$), consistent with dynamic exchange of IDR-bound Ferritin cores and very low concentrations of unbound FUS_N-SspB (Figures S3A–S3C), resulting in a system depicted in inset (I) of Figure 3C. However, as $\bar{f}$ approaches the binding capacity of cores (i.e., 24), this correspondence begins deviating (Figure 3D, $f_{Dilute} > 24$), suggesting the buildup of an unbound IDR population that partitions asymmetrically, as depicted in

inset (II) of Figure 3C. This core saturation appears to underlie an interesting feature of the phase diagram: as the number of IDRs per core increases (i.e., decreasing $\bar{f}^{-1}$), the right side of the binodal appears to pull back to lower core concentrations (Figure 3B). This effect becomes apparent at $\bar{f}^{-1} \approx 16$ (Figure 3B), similar to where f_{Dense} and f_{Dilute} begin deviating (Figure 3D). Consistent with this kink in the phase diagram reflecting core saturation by excess IDRs, when we plot the same phase diagrams as a function of the IDR concentration, we find no such decrease in IDR concentration in the dense phase, with the right side of the binodal exhibiting a nearly straight line on a semi-log plot, underscoring the central role of IDR-IDR interactions (Figure 3C). Strikingly, the left binodal arm exhibits a fixed IDR concentration, independent of the particular valency; for FUS_N Corelets, we estimate this value at 20.95 ± 7.66 μM (mean $\pm$ SD), with an estimated measurement accuracy of ~ 2-fold (STAR Methods).

These phase diagrams exhibit an additional feature consistent with phase separation theory (Berry et al., 2018): we find that cells expressing concentrations deep within the two-phase region exhibit early stage coarsening morphologies—connected network-like condensates—associated with spinodal decomposition (Cahn, 1961, 1965) while cells closer to the binodal boundary exhibit punctate nucleation and growth (Figures 4B and 4A, respectively; Videos S2 and S3, respectively). Moreover, for some highly expressing cells, we observe nucleation and growth of dilute-phase droplets within a continuous condensed phase, as expected on the right half of the two-phase regime of the phase diagram (Figure 4C; Video S4). These dilute phases fuse to one another, coarsen, and further fuse to nucleoli and nuclear lamina, while yielding condensates that may occupy a volume of over 70% of the nuclear volume (Figures 4C and S4F). Taken together, observing the condensation modes for each cell allows us to denote a region where spinodal decomposition is observable under the frame rate and resolution limits of the measurement and therefore estimate the approximate location of the spinodal boundary (Figure 4D).

Phase Diagrams Show Strong Dependence on Chemical Attributes of Protein Sequence

We next used the Corelet system to examine how specific chemical moieties within IDRs affect their phase diagrams (Brangwynne et al., 2015). We focused on the behavior of FUS, for which previous studies have underscored the key role of tyrosine (Y) residues in promoting phase separation of the purified protein (Kato et al., 2012; Lin et al., 2017; Wang et al., 2018). We expressed Corelets in which the IDR utilized is FUS_N with five of the twenty-seven tyrosine residues mutated to serine (FUS_N-5Y, see STAR Methods). In these cells, we find that phase separation is destabilized relative to FUS_N WT Corelets resulting in a downward shift of the binodal phase (Figure 5A), such that values of $\bar{f}$ that give rise to phase separation in FUS_N-WT

(D) Despite major concentration differences, IDR-to-Core concentration ratios in dilute, f_{Dilute}, and dense, f_{Dense}, phases are similar (compared to gray line of slope 1) as long as cores are not saturated (dashed line).

(E) Volume fractions predicted by lever-rule are consistent with volume fraction segmentation of dense (V_{Dense}, bright green) and dilute phases (V_{Nu}-V_{No}-V_{Dense}, dark green), where V_{Nu}, V_{No}, and V_{Dense} represent the relative confocal volume of the nucleus (within full line), nucleoli (within dashed line), and dense phase (bright green), respectively. a and b are defined in inset of (B). Equality shown via comparison to gray line of slope 1. Scale bars, 5 μm. Error bars are SD of measurement within segmented pixels. See Figure S4I for error bars for dilute phases and pre-activated cells.
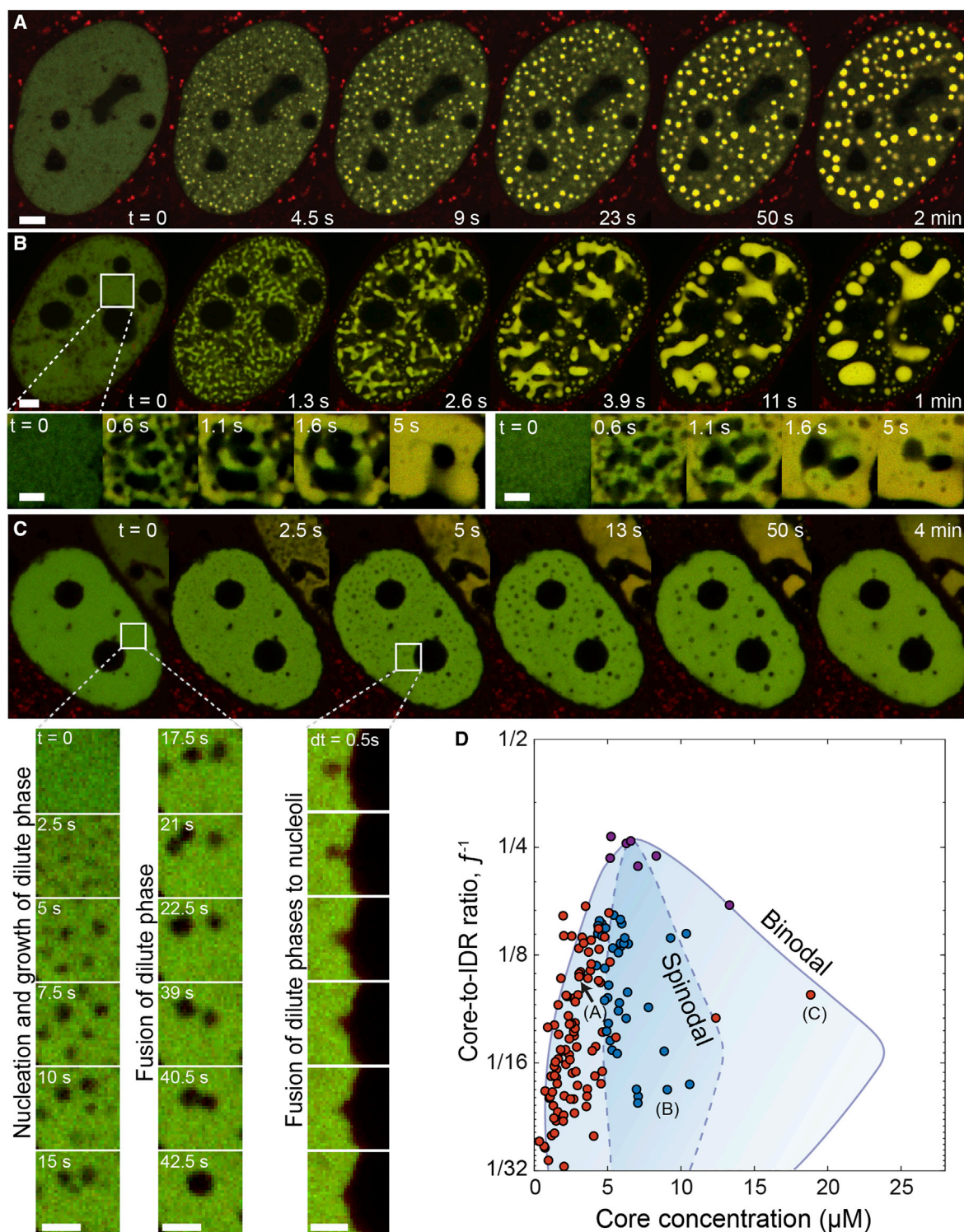
Figure 4. Distinct Modes of FUS$_N$ Corelet Phase Separation

(A) Phase separation via nucleation and growth occurs at low Core concentration. See Video S2.

(B) At intermediate Core concentration phase separation initiates with the rapid formation of elongated interconnected domains, as in spinodal decomposition. Insets: repeated activation of the same cellular region at higher time resolution showing differing morphology evolution. See Video S3.

(C) At very high Core concentration nucleation and growth of dilute phases within a dense phase was observed. Insets show enlarged nucleation (left) and subsequent fusion of dilute phases (center), as well as dilute phase fusion with a nucleolus (right). See Video S4.
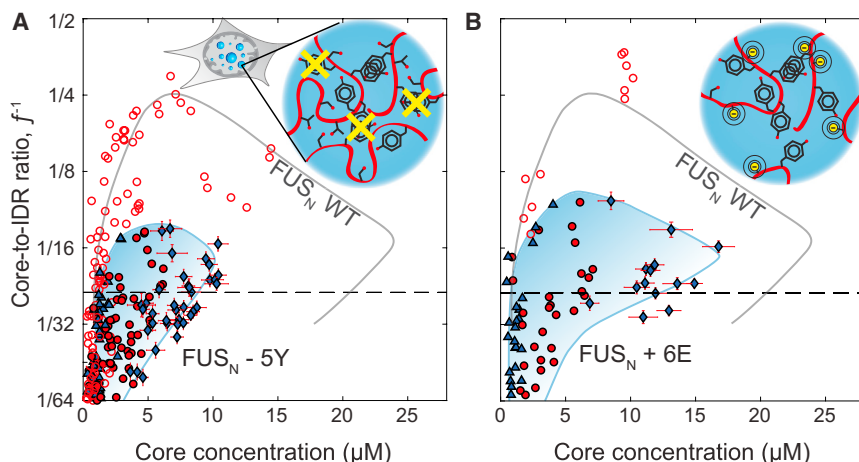
(legend continued on next page)

Figure 5. Phase Diagrams Show Strong Dependence on Chemical Attributes of Protein Sequence

(A) Phase diagram of FUS_N-5Y Corelets, with respect to Core concentration and Core-to-IDR ratio, f^{-1}. Symbols as in Figure 3B. Full valency line shown as dashed horizontal and FUS_N-WT Corelets binodal line from Figure 3B is shown in gray for comparison. Inset: schematic shows mutations removing a subset of FUS_N tyrosine residues (Y- > S).

(B) Phase diagram of phosphomimic FUS_N+6E Corelets. Inset: schematic of how S/T mutations to glutamic acid (E) introduce negative charge, as would phosphorylation of these sites. Axes, lines, and symbol definitions as in (A).

Error bars are SD of measurement within segmented pixels for dense phase. See also Figure S5.

Corelets no longer necessarily phase separate. Moreover, the condensates that do form in FUS_N-5Y Corelets are now significantly less concentrated than for WT FUS_N, due to a significant shift of the right arm of the binodal (Figure 5A). When all tyrosine residues in FUS_N where mutated to serine to study FUS_N-27Y Corelets, no distinct phases were observed; however, we do observe light-induced patterning associated with IDR-bound core exclusion from chromatin, an effect that is also observable with FUS_N constructs (Figures S5A and S5B, respectively).

We next looked at the role of phosphorylation in tuning IDR phase separation. Post translational modifications through phosphorylation has been shown to modulate phase separation, often diminishing or dissolving condensates through electrostatic repulsion between introduced phosphate groups (Han et al., 2012; Rai et al., 2018). In the FUS_N IDR, twelve serine (S) and threonine (T) residues are known to be subject to phosphorylation in response to DNA damage in living cells (Monahan et al., 2017). Substituting these twelve residues, or a subset of six, with glutamic acid as a phosphomimic has been shown to hinder FUS phase separation and gelation (Monahan et al., 2017). When we incorporate the FUS_N IDR with the same subset of S/T residues mutated to the negatively charged glutamic acid (E) (FUSN+6E, see STAR Methods), we find that the Corelet phase diagram is again significantly shifted down (Figure 5B), with the apparent critical point in the phase diagram adjusted to a much higher valence (lower $\bar{f}^{-1}$). Indeed, condensates that do form are now at much lower concentration (Figure 5B).

Concentration Amplification of IDRs Occurs through Diffusive Capture by Slowly Diffusing Cores

In the experiments described above, we define the activation zone over the entire nucleus of the cell under study. However, oc-

casionally only a fraction of adjacent cell nuclei was included in the activation zone. We noticed that in half-activated nuclei, droplets appear to be significantly larger close to the border between illuminated and non-illuminated fractions of the nucleus (Figure 6A). In cells illuminated with low power light (14 μW/μm^2), this effect becomes less prevalent, and the droplet size and number tend to be more evenly distributed throughout the activation zone, as shown for the half-illuminated cells expressing $HNRNPA1_C$ Corelets in Figure 6B. However, when we brightly half-illuminate nuclei (84 μW/μm^2) with low IDR module concentrations (in particular, low $\bar{f}$), we find that droplets form in a tight line at the illumination boundary (Figure 6B). Similar findings are observed with FUS_N (Figure 6C). Prior to droplet nucleation, the IDR concentration exhibits a peak at the boundary, with depletion into the non-illuminated region (Figure 6D, t = 5 s).

We reasoned that the IDR buildup at the illumination interface could occur because the Cores at the interface are accessible to and can readily capture IDR components diffusing in from the non-illuminated region. To quantitatively examine this physical picture, we developed a simple computational simulation in which IDRs are modeled as particles that can adhere to the surface of a larger core particle, which supports up to 24 bound IDRs (see STAR Methods). For low $\bar{f}$, activation of only half of the cell results in a large buildup of IDR particles at the activation interface, with a depletion in the non-activated region, as observed in experiments (Figure 6E; Video S5). Interestingly, the simulation suggests that this effect depends on the relative diffusivities, D, of the core and IDR particles: for higher ratios of D_{IDR}/D_{Core}, simulations show a significant local concentration buildup, while for D_{IDR}/D_{Core} close to unity, no buildup is observed (Figure 6E; Video S5). Using fluorescence correlation spectroscopy (FCS) to measure the Cores and IDR diffusivities

(D) Positioning phase separating cells according to their valence and core concentration at the time of activation and labeling them accordingly to the observed condensation mode delineate the binodal and minimal spinodal regions of the phase diagram. Red circles indicate average nuclear concentrations for which phase separation follows nucleation and growth of dense phases (left) or dilute phases (right), and blue circles are concentrations where spinodal decomposition is observed. Unlike the diagram in Figure 2D, points represent mean nuclear fluorescence upon activation (2 s after light activation). Purple symbols represent cells in which the exact condensation mode could not be conclusively determined (see Figure S5B). Binodal curves from Figure 2B. Approximate spinodal curve (dashed line) drawn to encapsulate average nuclear concentrations showing spinodal decomposition morphologies. Cells depicted in (A)–(C) are indicated. Scale bars, 2 μm for enlarged insets; 5 μm elsewhere.
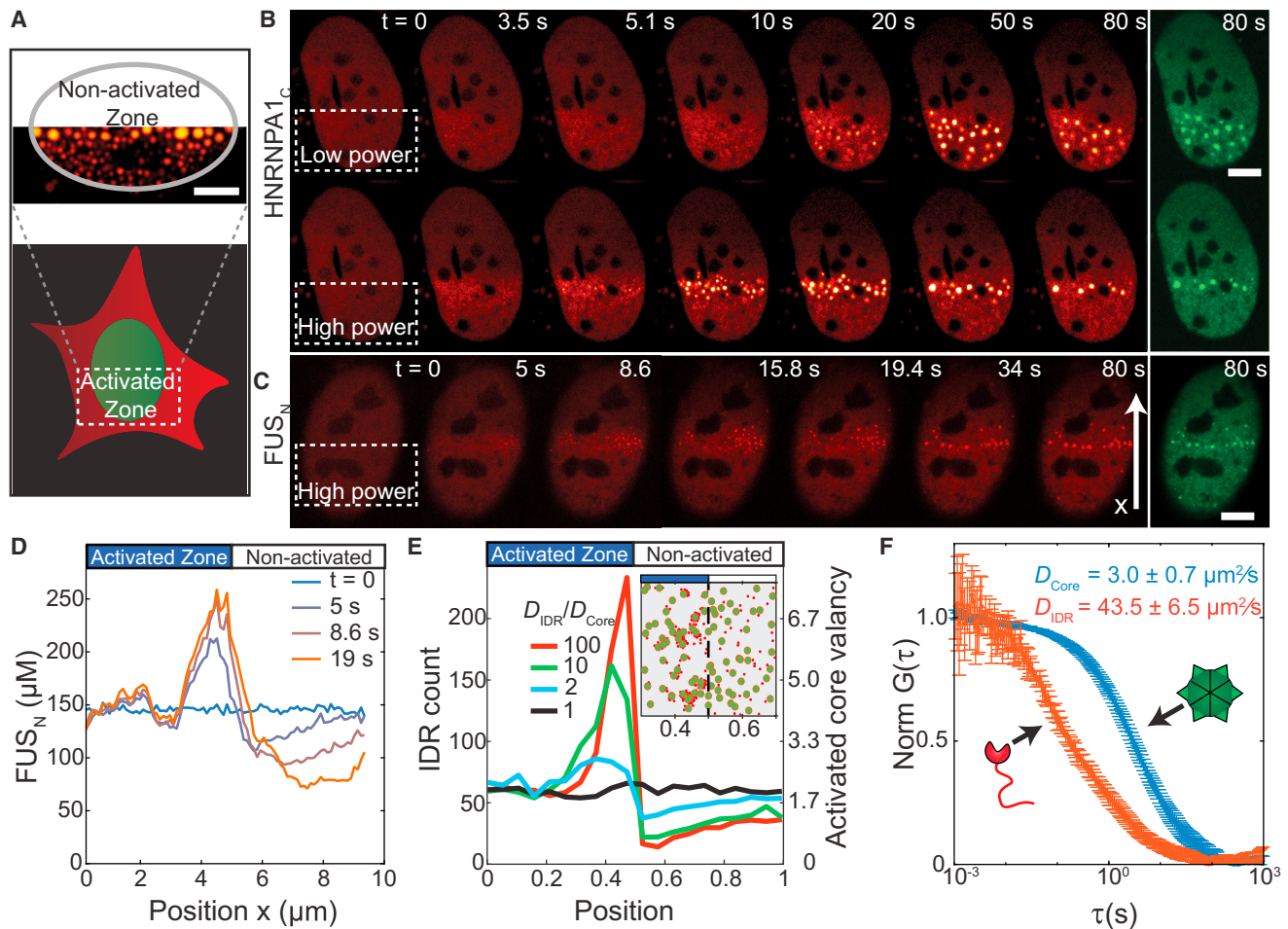
Figure 6. Concentration Amplification of IDRs Occurs through Diffusive Capture by Slowly Diffusing Cores

(A) Example image showing how activating a fraction of the cell nucleus leads to non-uniform droplet size-distribution.

(B and C) Time-lapse imaging of U2OS cell nuclei partially activated by low (14 $\mu W/\mu m^2$, top) or high (84 $\mu W/\mu m^2$, bottom) activation power. Low power yields uniform nucleation within activated zone, while high power yields preferential nucleation at the boundary between activated and non-activated zones for both HNRNPA1$_N$ (B) and (C) FUS$_N$-based Corelets in cell with $\bar{f}$ = 5.4 and [Core] = 4.1 μM. For (B) and (C), red panels are IDR channel, and green panels are Core channel, which was imaged in the last frame.

(D) Time-dependent FUS$_N$ concentration profiles across cell nucleus from (C) with the onset of high power half-cell photo-activation. FUS$_N$ molecules progressively accumulate at the activated zone boundary and are depleted within the non-activated zone.

(E) Simulation demonstrating that diffusive capture of IDR particles by multivalent cores is sufficient for local enrichment at the activation interface, but only if the Cores diffuse more slowly than IDRs. See Video S5. Inset: snapshot of a simulation with $D_{IDR}/D_{core} \cong 10$. Red, IDR particles; green, multivalent core.

(F) FCS normalized autocorrelation plots measured for core (blue) and IDR (FUS$_N$, red) components in the nucleoplasm. Error bars are SD of the autocorrelation function measured in different cells (n = 5).

Scale bars, 5 μm.

in living cell nuclei, we find that $D_{FUS} = 43.5 \pm 6.5$ $\mu m^2/s$, while the core diffusivity is significantly less, even without bound IDRs: $D_{Core} = 3.0 \pm 0.7$ $\mu m^2/s$, such that $D_{IDR}/D_{Core} > 10$ (Figure 6F). These data suggest that Cores act not only as multimerizing scaffolds, but upon local activation can serve as slowly diffusing IDR sinks. Through a "diffusive capture" mechanism, the cores thereby entrap IDRs as they rapidly diffuse in from the non-illuminated side of the nucleus, slowing their transport, and locally enriching them to drive phase separation. The more uniform IDR buildup and droplet condensation under weaker illumination (Figure 6B) thus results from the associated lower binding ca-

pacity of Cores, which therefore saturate at lower valency and allow IDRs to propagate deeper into the activated region, consistent with simulations in which cores can only bind a small number of IDRs (Video S5).

Amplified Phase Separation by Local Diffusive Capture

Because partial activation of the cell can give rise to gradients in IDR concentration and valency, we wondered what would happen with non-phase separating cells. In order to be sensitive to differences in local concentration, we first chose a cell with Core and IDR concentrations that position it close to the upper
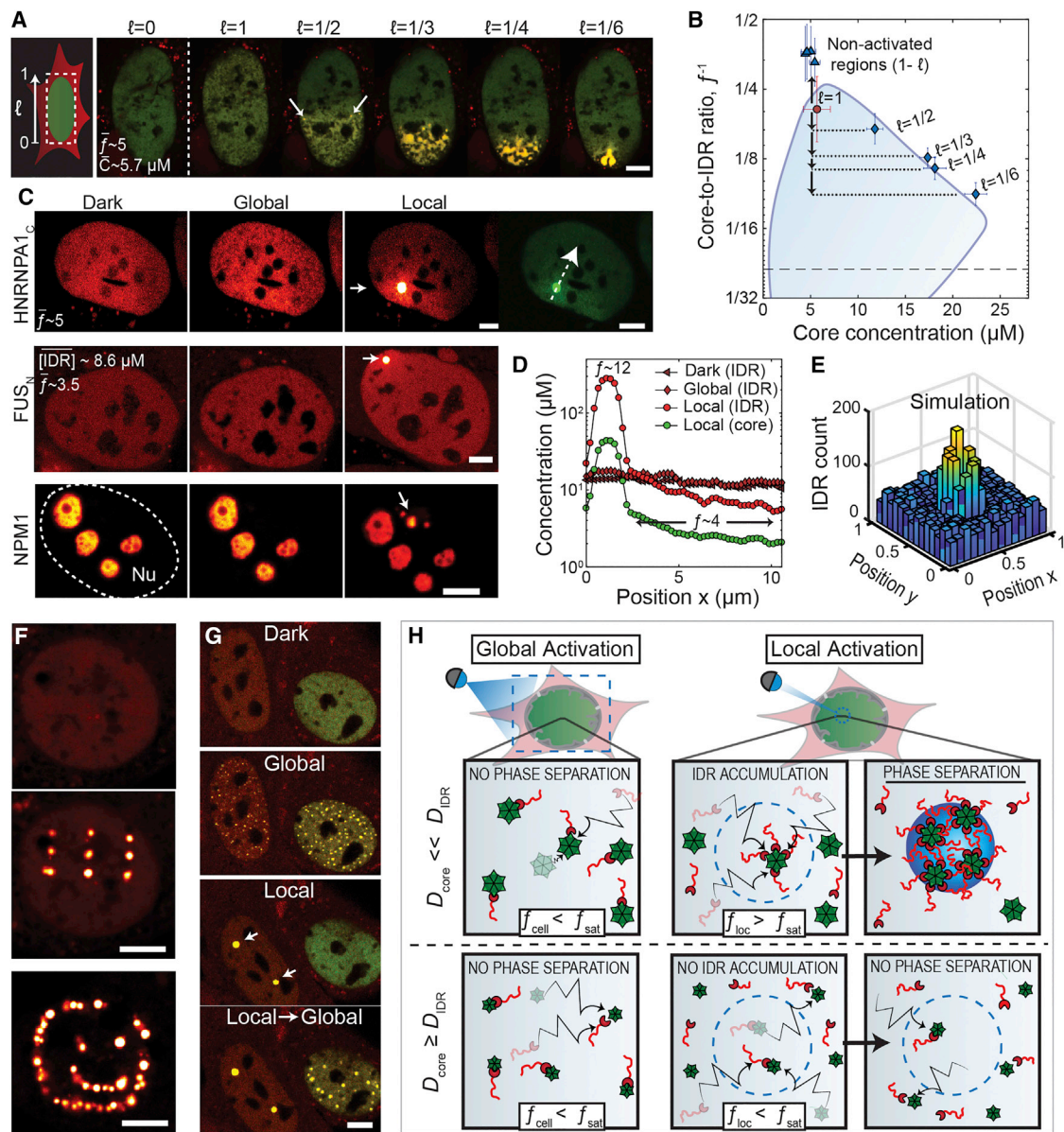
Figure 7. Amplified Phase Separation by Local Diffusive Capture

(A) Performing multiple on-off cycles on subfractions of a near-critical U2OS cell expressing FUS$_N$ Corelets gives rise to a gradually enhanced phase separation with increasingly concentrated condensates as size of activated nuclear region decreases. See Video S6.

(B) The smaller the activated zone, the deeper the cell locally plunges into the two-phase region, as compared to the average nuclear concentration (red circle). When mapped according to local valency and core concentration (diamonds), resulting condensates follow the binodal phase boundary (blue shaded region) shown in Figure 3B. Triangles correspond to non-activated regions of the nucleus. Error bars are SD of measurement within segmented pixels for the preactivated cell, dense phases, and dilute phases at the non-activated subregion.

(C) Photo-activating a 0.5-μm spot (arrow) in globally non-activatable cells, expressing either HNRNPA1$_N$ Corelets (top), FUS$_N$ Corelets (middle), or NPM1 Corelets (bottom). In each case, local activation drives local phase separation. Top and middle: U2OS cell. Bottom: HeLa cell.

(D) Concentration profiles across HNRNPA1$_N$ Corelets expressed in U2OS cell (as marked in GFP channel of C) before and immediately after 2 min of local activation, showing local enhancement in $\bar{f}$, and depletion in the non-activated zone (values of $\bar{f}$ labeled for measurements after activation).

(E) Simulations of locally activated spot of IDR-binding Core particles with $D_{IDR}/D_{core} \cong 10$ shows strong IDR enrichment, as observed in experiment.

(F) Patterned activation examples with FUS$_N$ Corelets in NIH 3T3 cells. See Video S7.

(G) Global activation causes FUS$_N$ droplets to condense in both cell nuclei (second panel). However, after local activation of two spots within the bottom cell (third panel), global activation of the entire cell does not initiate new nucleation events in that cell (fourth panel).

(legend continued on next page)

critical point on the phase diagram, such that spatial concentration variations, but no distinct condensates are observed upon uniform illumination (Figure 7A; Video S6). Consistent with diffusive capture and the resulting local concentration amplification, under half-cell activation, the nucleus indeed exhibits small distinct condensates (white arrows, Figure 7A). Moreover, for 1/3, 1/4, and 1/6 nuclear area activation, larger droplets are observed to condense in the activated region (Figure 7A; Video S6). The less circular morphologies observed as a result of these rapid excitation cycles again likely reflect an interplay with chromatin heterogeneities within the nucleus (Figure S5). Interestingly, as a smaller fraction of the nucleus is illuminated, the molar ratio inside droplets, f_{Dense}, is no longer the same as the average in the entire nucleus, $\bar{f}$, as only a fraction of the Cores are activated, which can nevertheless potentially capture a large fraction of the pool of IDRs rapidly diffusing throughout the nucleoplasm. Together with measurements of $[Core]_{Dense}$, we find that the droplets now correspond to points still on the binodal curve, but much deeper (lower $\bar{f}^{-1}$) within the two-phase region (Figure 7B). Moreover, regions outside of the activation zone now correspond to much lower values of $\bar{f}$ (Figure 7B). Thus, activating local regions of the cell gives rise to diffusive IDR capture and amplification of valence/concentration, causing local supersaturation sufficient for droplet condensation, even under globally dilute IDR concentrations.

We also see this effect—phase separation enhanced by local illumination—in Corelets formed from HNRNPA1$_C$, FUS$_N$, and the nucleolar protein NPM1, with very low nucleoplasmic concentrations (Figure 7C). Remarkably, FUS$_N$ Corelet cells can exhibit IDR concentrations as low as 2-fold below the IDR phase boundary (Figure 3C) and yet still phase separate upon local activation (Figure 7C). Because smaller activation zones are associated with a higher valence, this effect becomes particularly strong for highly localized activation. Indeed, by focusing light on a single diffraction limited spot, we find that we can drive highly localized droplet condensation (Figure 7D); simulations with localized activation support the physical picture of diffusive capture and concentration amplification with tight local activation (Figure 7E). Using patterned activation light, individual droplets could be written into different locations in the nucleus, to form 3 × 3 matrices and other arbitrary shapes (Figure 5F; Video S7). Moreover, in some cases where we locally activate a small number of single droplets, subsequent uniform illumination does not result in additional droplet condensation throughout the nucleoplasm (Figure 7G). This is consistent with the decreased $\bar{f}$ in these regions, which arises from activated Cores locally capturing IDRs and thereby depleting them from the non-activated regions.

DISCUSSION

Our results provide an unprecedented mapping of intracellular phase diagrams, which reveal a number of classical signatures associated with equilibrium phase diagrams, most remarkably droplet growth modes of nucleation and growth versus spinodal decomposition, defined by the nested binodal and spinodal phase boundaries. These findings thus provide strong evidence that the concepts of equilibrium liquid-liquid phase separation are indeed applicable within living cells. And yet, living cells are certainly out-of-equilibrium systems, and our ability to map these intracellular phase diagrams raises many questions about the role of non-equilibrium activity in liquid-liquid phase separation. Indeed, while we use the Corelet system to show that the N-terminal IDR of FUS (FUS$_N$) exhibits clear signatures of a near-equilibrium phase transition, this region of FUS is known to be subject to a number of post-translational modifications (PTMs) (Monahan et al., 2017). Our finding that the phosphomimetic FUS$_N$+6E construct exhibits a significantly shifted intracellular binodal boundary is consistent with little to no phosphorylation of the native FUS IDR, as previously suggested for unstressed cells (Monahan et al., 2017). These data support the concept that spatiotemporal changes to the average PTM state, for example under stress, during development or through the cell cycle (Rai et al., 2018), provide the cell with a set of handles to dynamically structure these phase diagrams for particular functional requirements.

The Corelet system reveals several interesting features of the non-equilibrium biophysics of patterned intracellular phase transitions. Most importantly, we identify a powerful mechanism by which slowly diffusing multivalent complexes can capture and amplify the concentration of associated IDR binding partners, and thus drive local condensation. The ability to locally concentrate IDRs is particularly interesting, given that the phase diagram (Figures 3B and 3C) shows that even a modest degree of oligomerization (i.e., the binding of ∼4 IDRs in the case of FUS$_N$) can promote phase separation. Thus, locally tuning multivalent interactions (e.g., through protein phosphorylation by spatially patterned kinases/phosphatases or the transcription of RNA as a local scaffold for IDP oligomerization) may be sufficient to drive local droplet condensation, even under conditions where the ligand (e.g., IDPs) are too dilute globally for phase separation to occur (Figure 7H). Mounting evidence supports the key role of IDP oligomerization in driving phase transitions (Aoki et al., 2018; Conicella et al., 2016; Feric et al., 2016; Mitrea et al., 2016; Tourrière et al., 2003) Oligomerization domains in locally activated IDPs will naturally give rise to slowly diffusing complexes capable of capturing additional unbound IDPs, suggesting the concentration amplification mechanism is likely at play in a broad array of biological condensates.

This diffusive capture mechanism may also be relevant for phase transitions involving nucleic acids, which are key components of many native IDP-rich intracellular condensates. DNA, mRNA, and lncRNA often exhibit extremely slow diffusion rates <1 μm^2/s and together with their ability to simultaneously bind multiple disordered proteins, would allow them to serve as potent nucleators of local phase separation. Diffusive capture is thus

(H) Schematic illustration of physical model of how local activation can drive a diffusive flux of IDR toward slowly diffusing cores scaffolds at the activation zone (dashed blue line), causing high local valency, f_{loc} that exceeds the saturation threshold, f_{sat}, for phase separation, and locally entering into the binodal phase space. In the case where Core and IDR diffusivities are similar, however, partially coated cores diffuse away from the activated region at the same rate as unbound IDRs and uncoated cores diffuse in, preventing f_{loc} from surpassing f_{sat}, yielding no phase separation.
Scale bars, 5 μm.

likewise a central mechanism in the emerging concept that liquid-liquid phase separation is involved in chromatin compaction and transcriptional control (Berry et al., 2015; Cho et al., 2018; Chong et al., 2018; Hnisz et al., 2017; Kwon et al., 2014; Larson et al., 2017; Sabari et al., 2018; Strom et al., 2017) that involves a dynamic collection of numerous types of DNA and RNA. Indeed, while associated IDRs and other condensation-promoting ligands are often not present at particularly high concentrations (Biggin, 2011), they are nevertheless known to specifically bind to multivalent nucleic acids throughout the nucleus.

Here, we focused on quantitatively elucidating the biophysics underlying patterned intracellular phase separation, but the biomimetic Corelet system will provide a powerful tool for examining other aspects of the physics of condensed biomolecular phases. It will also serve to inspire other optogenetic nucleation platforms (e.g., utilizing different multivalent core particles) or linear variants. These tools will find a broad range of uses, not only for interrogating fundamental cell biological questions, but also for synthetic biomaterials and organelle engineering applications. These approaches will increasingly synergize with those in materials science, for example in the design of bio-interfacing materials with novel properties arising from star-polymer architectures (Ren et al., 2016). Bioengineering of such structures and their interplay with fundamental studies on the non-equilibrium biophysics of intracellular phase transitions promises to be a fruitful area of future research.

STAR★METHODS

Detailed methods are provided in the online version of this paper and include the following:

- KEY RESOURCES TABLE
- CONTACT FOR REAGENT AND RESOURCE SHARING
- EXPERIMENTAL MODEL AND SUBJECT DETAILS
  - Cell culture
  - Yeast
  - Nematodes
- METHOD DETAILS
  - Plasmid construction
  - Construction of Corelet-expressing experimental models
  - Live cell imaging
  - Western blot for measurements of relative endogenous ferritin and engineered Core expression levels
- QUANTIFICATION AND STATISTICAL ANALYSIS
  - Determining diffusion coefficients and absolute concentrations for Corelets components
  - Image analysis and phase diagram construction
  - Fluorescence recovery after photobleaching analysis
  - Determination of Corelet spacing and occupancy in condensates
  - Simulations

SUPPLEMENTAL INFORMATION

Supplemental Information includes five figures and seven videos and can be found with this article online at https://doi.org/10.1016/j.cell.2018.10.048.

A video abstract is available at https://doi.org/10.1016/j.cell.2018.10.048#mmc8.

AUTHOR CONTRIBUTIONS

Conceptualization, D.B. and C.P.B.; Methodology, D.B., J.L.A., J.E.T., and C.P.B.; Software, D.B. and C.P.B.; Formal Analysis, D.B. and M.-T.W.; Investigation, D.B., M.T.W., M.-T.W., L.Z., M.K., and C.P.B.; Resources, J.L.A., J.E.T., and C.P.B.; Writing – Original Draft, Review, & Editing, D.B., M.T.W., and C.P.B.; Visualization, D.B., M.T.W., and C.P.B.; Supervision, C.P.B.; Funding Acquisition, J.L.A., J.E.T., and C.P.B.

DECLARATION OF INTERESTS

The authors declare no competing interests. A patent application describing the Corelet system is currently pending.

REFERENCES

Aoki, S.T., Crittenden, S.L., Lynch, T.R., Bingman, C.A., Wickens, M., and Kimble, J. (2018). Nematode germ granule assembly is linked to mRNA repression. bioRxiv. https://doi.org/10.1101/382838.

Asherie, N. (2004). Protein crystallization and phase diagrams. Methods 34, 266–272.

Banani, S.F., Lee, H.O., Hyman, A.A., and Rosen, M.K. (2017). Biomolecular condensates: organizers of cellular biochemistry. Nat. Rev. Mol. Cell Biol. 18, 285–298.

Bellapadrona, G., and Elbaum, M. (2014). Supramolecular protein assemblies in the nucleus of human cells. Angew. Chem. Int. Ed. Engl. 53, 1534–1537.

Berry, J., Weber, S.C., Vaidya, N., Haataja, M., and Brangwynne, C.P. (2015). RNA transcription modulates phase transition-driven nuclear body assembly. Proc. Natl. Acad. Sci. USA 112, E5237–E5245.

Berry, J., Brangwynne, C.P., and Haataja, M. (2018). Physical principles of intracellular organization via active and passive phase transitions. Rep. Prog. Phys. 81, 046601.

Biggin, M.D. (2011). Animal transcription networks as highly connected, quantitative continua. Dev. Cell 21, 611–626.

Brangwynne, C.P., Eckmann, C.R., Courson, D.S., Rybarska, A., Hoege, C., Gharakhani, J., Jülicher, F., and Hyman, A.A. (2009). Germline P granules are liquid droplets that localize by controlled dissolution/condensation. Science 324, 1729–1732.

Brangwynne, C.P., Mitchison, T.J., and Hyman, A.A. (2011). Active liquid-like behavior of nucleoli determines their size and shape in Xenopus laevis oocytes. Proc. Natl. Acad. Sci. USA *108*, 4334–4339.

Brangwynne, C.P., Tompa, P., and Pappu, R.V. (2015). Polymer physics of intracellular phase transitions. Nat. Phys. *11*, 899–904.

Broide, M.L., Berland, C.R., Pande, J., Ogun, O.O., and Benedek, G.B. (1991). Binary-liquid phase separation of lens protein solutions. Proc. Natl. Acad. Sci. USA *88*, 5660–5664.

Cahn, J.W. (1961). On spinodal decomposition. Acta Metall. *9*, 795–801.

Cahn, J.W. (1965). Phase separation by spinodal decomposition in isotropic systems. J. Chem. Phys. *42*, 93–99.

Cho, W.-K., Spille, J.-H., Hecht, M., Lee, C., Li, C., Grube, V., and Cisse, I.I. (2018). Mediator and RNA polymerase II clusters associate in transcription-dependent condensates. Science *361*, 412–415.

Choi, W., Fang-Yen, C., Badizadegan, K., Oh, S., Lue, N., Dasari, R.R., and Feld, M.S. (2007). Tomographic phase microscopy. Nat. Methods *4*, 717–719.

Chong, S., Dugast-Darzacq, C., Liu, Z., Dong, P., Dailey, G.M., Cattoglio, C., Heckert, A., Banala, S., Lavis, L., Darzacq, X., et al. (2018). Imaging dynamic and selective low-complexity domain interactions that control gene transcription. Science *361*, eaar2555.

Conicella, A.E., Zerze, G.H., Mittal, J., and Fawzi, N.L. (2016). ALS mutations disrupt phase separation mediated by α-helical structure in the TDP-43 low-complexity C-terminal domain. Structure *24*, 1537–1549.

Dill, K.A., and Bromberg, S. (2011). Molecular Driving Forces: Statistical Thermodynamics in Biology, Chemistry, Physics, and Nanoscience (CRC Press).

Dundr, M., and Misteli, T. (2010). Biogenesis of nuclear bodies. Cold Spring Harb. Perspect. Biol. *2*, a000711.

Elbaum-Garfinkle, S., Kim, Y., Szczepaniak, K., Chen, C.C.-H., Eckmann, C.R., Myong, S., and Brangwynne, C.P. (2015). The disordered P granule protein LAF-1 drives phase separation into droplets with tunable viscosity and dynamics. Proc. Natl. Acad. Sci. USA *112*, 7189–7194.

Entian, K.-D., and Kötter, P. (2007). Yeast genetic strain and plasmid collections. Methods Microbiol. *36*, 629–666.

Falahati, H., Pelham-Webb, B., Blythe, S., and Wieschaus, E. (2016). Nucleation by rRNA dictates the precision of nucleolus assembly. Curr. Biol. *26*, 277–285.

Feric, M., Vaidya, N., Harmon, T.S., Mitrea, D.M., Zhu, L., Richardson, T.M., Kriwacki, R.W., Pappu, R.V., and Brangwynne, C.P. (2016). Coexisting liquid phases underlie nucleolar subcompartments. Cell *165*, 1686–1697.

Gibson, D.G., Young, L., Chuang, R.-Y., Venter, J.C., Hutchison, C.A., 3rd, and Smith, H.O. (2009). Enzymatic assembly of DNA molecules up to several hundred kilobases. Nat. Methods *6*, 343–345.

Guntas, G., Hallett, R.A., Zimmerman, S.P., Williams, T., Yumerefendi, H., Bear, J.E., and Kuhlman, B. (2015). Engineering an improved light-induced dimer (iLID) for controlling the localization and activity of signaling proteins. Proc. Natl. Acad. Sci. USA *112*, 112–117.

Han, T.W., Kato, M., Xie, S., Wu, L.C., Mirzaei, H., Pei, J., Chen, M., Xie, Y., Allen, J., Xiao, G., and McKnight, S.L. (2012). Cell-free formation of RNA granules: bound RNAs identify features and components of cellular assemblies. Cell *149*, 768–779.

Hnisz, D., Shrinivas, K., Young, R.A., Chakraborty, A.K., and Sharp, P.A. (2017). A phase separation model for transcriptional control. Cell *169*, 13–23.

Honerkamp-Smith, A.R., Veatch, S.L., and Keller, S.L. (2009). An introduction to critical points for biophysicists; observations of compositional heterogeneity in lipid membranes. Biochim. Biophys. Acta *1788*, 53–63.

Kato, M., Han, T.W., Xie, S., Shi, K., Du, X., Wu, L.C., Mirzaei, H., Goldsmith, E.J., Longgood, J., Pei, J., et al. (2012). Cell-free formation of RNA granules: low complexity sequence domains form dynamic fibers within hydrogels. Cell *149*, 753–767.

Krichevsky, O., and Gregoire, B. (2002). Fluorescence correlation spectroscopy: the technique and its applications. Rep. Prog. Phys. *65*, 251–297.

Kwon, I., Kato, M., Xiang, S., Wu, L., Theodoropoulos, P., Mirzaei, H., Han, T., Xie, S., Corden, J.L., and McKnight, S.L. (2014). Phosphorylation-regulated

binding of RNA polymerase II to fibrous polymers of low-complexity domains. Cell *155*, 1049–1060.

Larson, A.G., Elnatan, D., Keenen, M.M., Trnka, M.J., Johnston, J.B., Burlingame, A.L., Agard, D.A., Redding, S., and Narlikar, G.J. (2017). Liquid droplet formation by HP1α suggests a role for phase separation in heterochromatin. Nature *547*, 236–240.

Li, P., Banjade, S., Cheng, H.-C., Kim, S., Chen, B., Guo, L., Llaguno, M., Hollingsworth, J.V., King, D.S., Banani, S.F., et al. (2012). Phase transitions in the assembly of multivalent signalling proteins. Nature *483*, 336–340.

Lin, Y., Currie, S.L., and Rosen, M.K. (2017). Intrinsically disordered sequences enable modulation of protein phase separation through distributed tyrosine motifs. J. Biol. Chem. *292*, 19110–19120.

Loman, A., Dertinger, T., Koberling, F., and Enderlein, J. (2008). Comparison of optical saturation effects in conventional and dual-focus fluorescence correlation spectroscopy. Chem. Phys. Lett. *459*, 18–21.

Mitrea, D.M., Cika, J.A., Guy, C.S., Ban, D., Banerjee, P.R., Stanley, C.B., Nourse, A., Deniz, A.A., and Kriwacki, R.W. (2016). Nucleophosmin integrates within the nucleolus via multi-modal interactions with proteins displaying R-rich linear motifs and rRNA. eLife *5*, 1–33.

Monahan, Z., Ryan, V.H., Janke, A.M., Burke, K.A., Rhoads, S.N., Zerze, G.H., O'Meally, R., Dignon, G.L., Conicella, A.E., Zheng, W., et al. (2017). Phosphorylation of the FUS low-complexity domain disrupts phase separation, aggregation, and toxicity. EMBO J. *36*, 2951–2967.

Müller, C.B., Eckert, T., Loman, A., Enderlein, J., and Richtering, W. (2009). Dual-focus fluorescence correlation spectroscopy: a robust tool for studying molecular crowding. Soft Matter *5*, 1358.

Nakamura, H., Lee, A.A., Afshar, A.S., Watanabe, S., Rho, E., Razavi, S., Suarez, A., Lin, Y.C., Tanigawa, M., Huang, B., et al. (2018). Intracellular production of hydrogels and synthetic RNA granules by multivalent molecular interactions. Nat. Mater. *17*, 79–89.

Nott, T.J., Petsalaki, E., Farber, P., Jervis, D., Fussner, E., Plochowietz, A., Craggs, T.D., Bazett-Jones, D.P., Pawson, T., Forman-Kay, J.D., and Baldwin, A.J. (2015). Phase transition of a disordered nuage protein generates environmentally responsive membraneless organelles. Mol. Cell *57*, 936–947.

Petrásek, Z., and Schwille, P. (2008). Precise measurement of diffusion coefficients using scanning fluorescence correlation spectroscopy. Biophys. J. *94*, 1437–1448.

Rai, A.K., Chen, J.-X., Selbach, M., and Pelkmans, L. (2018). Kinase-controlled phase transition of membraneless organelles in mitosis. Nature *559*, 211–216.

Ren, J.M., McKenzie, T.G., Fu, Q., Wong, E.H.H., Xu, J., An, Z., Shanmugam, S., Davis, T.P., Boyer, C., and Qiao, G.G. (2016). Star Polymers. Chem. Rev. *116*, 6743–6836.

Rubinstein, M., and Colby, R.H. (2003). Polymer Physics (Oxford University Press).

Sabari, B.R., Dall'Agnese, A., Boija, A., Klein, I.A., Coffey, E., Shrinivas, K., Abraham, B.J., Hannett, N.M., Zamudio, A.V., Manteiga, J.C., et al. (2018). Coactivator condensation at super-enhancers links phase separation and gene control. Science *361*, eaar3958.

Shin, Y., and Brangwynne, C.P. (2017). Liquid phase condensation in cell physiology and disease. Science *357*, eaaf4382.

Shin, Y., Berry, J., Pannucci, N., Haataja, M.P., Toettcher, J.E., and Brangwynne, C.P. (2017). Spatiotemporal control of intracellular phase transitions using light-activated optodroplets. Cell *168*, 159–171.

Smith, J., Calidas, D., Schmidt, H., Lu, T., Rasoloson, D., and Seydoux, G. (2016). Spatial patterning of P granules by RNA-induced phase separation of the intrinsically-disordered protein MEG-3. eLife *5*, 1–18.

Strom, A.R., Emelyanov, A.V., Mir, M., Fyodorov, D.V., Darzacq, X., and Karpen, G.H. (2017). Phase separation drives heterochromatin domain formation. Nature *547*, 241–245.

Tourrière, H., Chebli, K., Zekri, L., Courselaud, B., Blanchard, J.M., Bertrand, E., and Tazi, J. (2003). The RasGAP-associated endoribonuclease G3BP assembles stress granules. J. Cell Biol. *160*, 823–831.

Wang, J., Choi, J.M., Holehouse, A.S., Lee, H.O., Zhang, X., Jahnel, M., Maharana, S., Lemaitre, R., Pozniakovsky, A., Drechsel, D., et al. (2018). A molecular grammar governing the driving forces for phase separation of prion-like RNA binding proteins. Cell *174*, 688–699.

Wei, M.T., Elbaum-Garfinkle, S., Holehouse, A.S., Chen, C.C.H., Feric, M., Arnold, C.B., Priestley, R.D., Pappu, R.V., and Brangwynne, C.P. (2017). Phase behaviour of disordered proteins underlying low density and high permeability of liquid organelles. Nat. Chem. *9*, 1118–1125.

West, J.A., Davis, C.P., Sunwoo, H., Simon, M.D., Sadreyev, R.I., Wang, P.I., Tolstorukov, M.Y., and Kingston, R.E. (2014). The long noncoding RNAs NEAT1 and MALAT1 bind active chromatin sites. Mol. Cell *55*, 791–802.

Zhu, L., and Brangwynne, C.P. (2015). Nuclear bodies: the emerging biophysics of nucleoplasmic phases. Curr. Opin. Cell Biol. *34*, 23–30.

Zwicker, D., Decker, M., Jaensch, S., Hyman, A.A., and Jülicher, F. (2014). Centrosomes are autocatalytic droplets of pericentriolar material organized by centrioles. Proc. Natl. Acad. Sci. USA *111*, E2636–E2645.

STAR★METHODS

KEY RESOURCES TABLE

REAGENT or RESOURCE	SOURCE	IDENTIFIER
Antibodies		
Anti-β-Actin Antibody, Rabbit	abcam	Cat#ab8227; RRID: AB_2305186
Anti-Ferritin Heavy Chain Antibody, Mouse	Millipore Sigma	Cat#MABC602; RRID: AB_2734745
Anti-Rabbit IgG, Peroxidase Conjugated, Goat	Jackson ImmunoResearch Labs	Cat#111-035-144; RRID: AB_2307391
Anti-Mouse IgG, Peroxidase Conjugated, Goat	Jackson ImmunoResearch Labs	Cat#115-035-062; RRID: AB_2338504
Bacterial and Virus Strains		
E. coli, Stellar Competent Cells, HST08	Takara Bio USA	Cat#636766
Chemicals, Peptides, and Recombinant Proteins		
Lipofectamine 3000 Transfection Reagent	Invitrogen	Cat#E2311
FuGENE HD Transfection Reagent	Promega	Cat#L3000
GIBCO DMEM, High Glucose	Thermo Fisher Scientific	Cat#11-965-118
Fetal Bovine Serum, Premium, Heat-Inactivated	Atlanta Biologicals	Cat#S11150H
GIBCO Penicillin-Streptomycin (10,000 U/mL)	Thermo Fisher Scientific	Cat#15140122
In-Fusion HD Cloning	Takara Bio USA	Cat#638910
Fibronectin bovine plasma	Millipore Sigma	Cat#F1141
Hoechst 33342	Thermo Fisher Scientific	Cat#H1399
FTH1, Ferritin Heavy Chain, Human	Prospec-Tany Technogene	Cat#PRO-658
FTL, Ferritin Light Chain, Human	Prospec-Tany Technogene	Cat#PRO-650
Critical Commercial Assays		
Bradford Reagent	Millipore Sigma	Cat#B6916
SuperSignal West Pico Chemiluminescent Substrate	Thermo Fisher Scientific	Cat#34077
Protein Standard II, Bovine serum albumin	Bio-Rad	Cat#500-0007
Experimental Models: Cell Lines		
Human: Lenti-X 293T	Takara Bio USA	Cat#632180
Human: HEK293	Marc Diamond Lab, UT Southwestern	RRID:CVCL_0045
Human: U2OS	Tom Muir Lab, Princeton University	RRID:CVCL_0042
Human: HeLa	ATCC	RRID:CVCL_0058
Mouse: NIH 3T3	ATCC	RRID:CVCL_0594
HEK293+M22, M23	This paper	N/A
U2OS+M22, M23	This paper	N/A
U2OS+M43, M23	This paper	N/A
U2OS+M22, M28	This paper	N/A
U2OS+M22, M30	This paper	N/A
U2OS+M22, M31	This paper	N/A
HEK293+M22, M29	This paper	N/A
U2OS+M22, M60	This paper	N/A
U2OS+M22, M66	This paper	N/A
HeLa+M22, LZ231	This paper	N/A
NIH 3T3+ M22, M23	This paper	N/A
U2OS+M22, M27	This paper	N/A
U2OS+M22, M23, M49	This paper	N/A
U2OS+M22, M23, pBFP	This paper	N/A

(Continued on next page)

Continued

REAGENT or RESOURCE	SOURCE	IDENTIFIER
U2OS+M22, M63	This paper	N/A
HEK293+M23	This paper	N/A
HEK293+pMW043	This paper	N/A
Experimental Models: Organisms/Strains		
S. cerevisiae: CEN.PK-1C: *MATa*; *his3D1*; *leu2-3_112*; *ura3-52*; *trp1-289*; *MAL2-8c*; *SUC2*	Entian and Kötter, 2007	Euroscarf#30000A
C. elegans: Unc-119: *unc-119(ed3) III*	Brangwynne Lab	WormBase#HT1593
S. cerevisiae: JAy570: CEN.PK2+pMW012, pMW014	This paper	N/A
C. elegans: CPB205: Unc-119, allele ptnIs136 [dao-5p::LOV2::mTagBFP2::FTH1::tbb-2 3′UTR, *unc-119*]	This paper	N/A
C. elegans: CPB207: Unc-119, allele ptnIs138[pgl-1p::pgl-1::mCherry::sspB, *unc-119*]	This paper	N/A
C. elegans: CPB211: CBP205xCPB207	This paper	N/A
Recombinant DNA		
CDS: iLID	Guntas et al., 2015	Addgene Plasmid #60413
CDS: SspB	Guntas et al., 2015	Addgene Plasmid #60415
CDS: FTH1, Human	HEK293 cDNA Library	N/A
CDS: FUS_N: FUS_{1-214}, Human	Shin et al., 2017	N/A
CDS: $HNRNPA1_C$: $hnRNPA1_{186-320}$, Human	Shin et al., 2017	N/A
CDS: $DDX4_N$: $DDX4_{1-236}$, Human	Shin et al., 2017	N/A
CDS: $TDP-43_C$: $TDP-43_{218-414}$, Human	HEK293 cDNA Library	N/A
CDS: Human NPM1 Gene cDNA clone	Sino Biological	Cat#HG12074-G
CDS: GFP	Brangwynne Lab	N/A
CDS: mCherry	Shin et al., 2017	N/A
CDS: mTagBFP2 Gene Fragment	Integrated DNA Technologies (IDT)	N/A
CDS: FUS_N-5YS	IDT	N/A
CDS: FUS_N-27YS	IDT	N/A
CDS: FUS_N-6(S/T)E	IDT	N/A
Plasmid: pCMV-dR8.91	Toettcher Lab	N/A
Plasmid: pMD2.G	Toettcher Lab	N/A
Plasmid: pHR-SFFVp vector	Shin et al., 2017	N/A
Plasmid: pJLA122_0202: TEF1p-MCS-ACT1t, 2u vector, URA3 marker	Avalos Lab	N/A
Plasmid: pJLA121_0103: GPD1p-MCS-ADH1t, 2μ vector, URA3 marker	Avalos Lab	N/A
Plasmid: pJLA122_0103: GPD1p-MCS-ADH1t, 2u vector, LEU2 marker	Avalos Lab	N/A
Plasmid: M22: pHR-SFFVp-NLS-iLID::EGFP::FTH1	This paper	N/A
Plasmid: M23: pHR-SFFVp-FUS_N::mCherry::SspB	This paper	N/A
Plasmid: M27: pHR-SFFVp-mCherry::SspB	This paper	N/A
Plasmid: M28: pHR-SFFVp-FUS_FL::mCherry::SspB	This paper	N/A
Plasmid: M29: pHR-SFFVp-$DDX4_N$::mCherry::SspB	This paper	N/A
Plasmid: M30: pHR-SFFVp- $HNRNPA1_C$::mCherry::SspB	This paper	N/A
Plasmid: M31: pHR-SFFVp- $TDP-43_C$::mCherry::SspB	This paper	N/A
Plasmid: M43: pHR-SFFVp-iLID::EGFP::FTH1	This paper	N/A
Plasmid: M49: pHR-SFFVp- FUS_N::mTagBFP2	This paper	N/A
Plasmid: M60: pHR-SFFVp- FUS_N-5YS::mCherry::SspB	This paper	N/A

Continued

REAGENT or RESOURCE	SOURCE	IDENTIFIER
Plasmid: M63: pHR-SFFVp- FUS$_N$-27YS::mCherry::SspB	This paper	N/A
Plasmid: M67: pHR-SFFVp- FUS$_N$-6(S/T)E::mCherry::SspB	This paper	N/A
Plasmid: LZ231: pHR-SFFVp- NPM1::mCherry::SspB	This paper	N/A
Plasmid: pBFP pLV_sgTelomere_PuroR-T2A-mTagBFP2	Brangwynne Lab	N/A
Plasmid: pMW011: pJLA121_0202 TEF1p-iLID::EGFP::FTH1-ACT1t	This paper	N/A
Plasmid: pMW012: pJLA121_0103 GPD1p-FUS$_N$::mCherry::SspB-ADH1t	This paper	N/A
Plasmid: pMW014: pJLA122_0202 TEF1p-iLID::EGFP::FTH1-ACT1t	This paper	N/A
Plasmid: pMW043: pHR-SFFVp-EGFP-P2A-mCherry	This paper	N/A
Software and Algorithms		
Matlab2017b	Mathworks	https://www.mathworks.com/products/matlab.html
ImageJ2	NIH	https://imagej.nih.gov/ij/
SymPhoTime 64, version 2.1	PicoQuant	https://www.picoquant.com/products/category/software/symphotime-64-fluorescence-lifetime-imaging-and-correlation-software

CONTACT FOR REAGENT AND RESOURCE SHARING

Further information and requests for resources and reagents should be directed to and will be fulfilled by the Lead Contact, Clifford P. Brangwynne (cbrangwy@princeton.edu).

EXPERIMENTAL MODEL AND SUBJECT DETAILS

Cell culture

Human cell lines used in this study include Lenti-X 293T (Takara Bio USA, Sex: Female), HEK293 (Sex: Female), HeLa (ATCC, Sex: Female), and U2OS (Sex: Female). Lenti-X 293T cells were only utilized for virus preparation, while all others were used for experiments. The HEK293 cell line was authenticated by ATCC yielding at 81% match to ATCC HEK293 cells (CAT#CRL-1573). *Mus musculus* cell line NIH 3T3 (ATCC, Sex: Male) was additionally used in experiments.

Cells were cultured in 10% FBS (Atlanta Biological) DMEM (GIBCO) supplemented with penicillin and streptomycin at 37°C with 5% CO_2 in a humidified incubator. 1 day prior to imaging, cultured cells were trypsinized, quenched with medium, and plated on a 35-mm glass-bottom dish (MatTek) pre-coated for 20 min with PBS buffer containing 0.25 mg/ml fibronectin (Thermo). Hoechst Dye, stored as 10 mg/mL solution at −20°C, was thawed, diluted 1:2000 in culture medium and used in exchange with dye-free medium directly prior to imaging in glass-bottom dish for visualized of chromatin.

Yeast

The CEN.PK2-1C strain of *Saccharomyces cerevisiae* (Entian and Kötter, 2007, Euroscarf#30000A, Genotype: CEN.PK-1C MATa; his3D1; leu2-3_112; ura3-52; trp1-289; MAL2-8c; SUC2) was used in this study. For live-yeast imaging, single colonies were selected and grown in synthetic complete medium with 2% (w/v) glucose without leucine or uracil supplements (SC-Leu-Ura) overnight at 30°C, reseeded in SC-Leu-Ura media at OD_{600} of approximately 1.0 and grown at 30°C until mid-log phase (OD_{600} = 2.5-3.0) for imaging. Cells were briefly spun down at 3000 RPM for 5 min. The pellet was lightly resuspended in the supernatant; 4 μl was applied to a 3% agarose pad on a glass objective and sealed with a coverslip.

Nematodes

The Unc-119 strain of *Caenorhabditis elegans* (WormBase#HT1593, Genotype: unc-119(ed3) III) was used in this study. Worms were grown on 7 mm agar plates seeded with OP50 bacterial lawns at 20°C. Worms were transferred periodically either by chunking onto fresh plate using a flame sterilized metal blade, or by individual picking several worms using a flame sterilized metal pick. For imaging, embryos were dissected from gravid mothers in standard M9 buffer solution (3 g KH2PO4, 6 g Na2HPO4, 0.5 g NaCl, 1 g NH4Cl per 1 L) at room temperature, mounted on 3% agarose pads, and sealed with a coverslip.

METHOD DETAILS

Plasmid construction
For expression in cell culture
DNA constructs used for tissue culture were cloned using In-Fusion HD cloning kit (Clonetech) in a standard reaction mixture comprising 20 ng of each 1-3 PCR-amplified inserts or recombinant DNA gene blocks (gBlocks gene fragments, IDT) and 40 ng linearized pHR-SFFV backbone in a 5 μl reaction set to 50°C for 15 min. PCR fragments were produced using a standard PCR reaction using Phusion High-Fidelity DNA Polymerase (NEB). Oligonucleotides were synthesized by IDT. NLS sequence from Gallus gallus ferritoid (Bellapadrona and Elbaum, 2014) was incorporated by sequential PCR reactions. PCR products were purified using PCR purification kit (QIAGEN) and verified on an agarose gel. pHR-SFFV backbone was linearized using BamHI-HF and NotI-HF (NEB) following the manufacturer's instructions. Plasmids were transformed into Stellar cells (Clontech), from which single colonies were picked, grown in LB supplemented by Ampicillin overnight, and minipreped (QIAGEN) following manufacturer instructions. All cloning products were confirmed by sequencing (GENEWIZ).

Recombinant DNA gene blocks were obtained for iLID, SspB, FUS_N, FUS_N-5Y, −27Y, and +6E. FUS_N-5Y harbored tyrosine to serine mutations at Y17, Y75, Y81, Y143, Y149 (Kato et al., 2012). FUS_N-27Y harbored tyrosine to serine mutations at Y6, Y14, Y17, Y25, Y33, Y38, Y41, Y50, Y55, Y58, Y66, Y75, Y81, Y91, Y97, Y100, Y113, Y122, Y130, Y136, Y143, Y149, Y155, Y161, Y177, Y194, and Y208. FUS_N+6E harbored mutations to glutamic acid at S36, S30, T68, S84, S88, and S117 (Monahan et al., 2017).
For expression in S. cerevisiae
M22 and M23 constructs were cloned into pJLA121_0202 and pJLA121_0103 with Gibson isothermal assembly (Gibson et al., 2009), yielding pMW011 and pMW012, respectively. To change the auxotrophic marker, the TEF1p-iLID::EGFP::FTH1-ACT1t gene from pMW011 was inserted into the pJLA122_0103 backbone via restriction cloning with XmaI and AscI and ligation with T4 ligase (NEB).

Construction of Corelet-expressing experimental models
Cell lines
Corelet construct-containing Lentiviruses were produced by cotransfecting HEK293T cells plated on a 6-well plate for 24 hr with the desired DNA constructs (1.25 μg), pCMVdR8.91 (1.1 μg), and pMD2.G (0.15 μg) using Lipofectamine 3000 (Invitrogen) or FuGENE HD (Promega) following manufacturer instructions. 2 mL of viral supernatants were collected and filtered from cell debris using 0.45 μm filter (Fisher Scientific) within 2-3 days following transfection. HEK293, U2OS, and NIH 3T3 cells were transduced while at 60% confluency on 6-well plates by adding 0.3-1.5 mL of each of the harvested Lentiviruses to the cell medium in accordance with the desirable expression levels of Cores and IDRs in the various experiment. Apart from cells with core conc higher than ~10 μM (where we observe slow cell division rate), cell viability appears to be unaffected by Corelet expression.
Yeast
2μ plasmids pMW012 and pMW014 were simultaneously transformed into the CEN.PK2-1C strain of S. cerevisiae using standard lithium acetate protocol and screened for on SC-Ura-Leu Agar plates with 2% (w/v) glucose
Nematodes
C. elegans expressing LOV2::mTagBFP2::FTH1 driven by dao5 promoter were established by mosSCI (CPB205)]. Worms expressing PGL-1::mCherry::SspB (CPB207 were generated using CRISPR/Cas9 and driven by the endogenous promoter. CPB 205 and CPB 207 were crossed to create CPB 211[ptnIs136; ptnIs138], the PGL-1 Corelet line. To cross CPR205 and 207, male worms for a desired strain were generated at higher than baseline levels by applying him17 RNAi treatment to L4 worms and subsequently identifying males produced in the next generation. Crosses were then set up on unseeded plates where a dense yet small spot of OP50 was placed in order to increase contact frequency between males and hermaphrodites. Ideally, approximately 10 males and 5 hermaphrodites were used for each cross. Young L3/L4 hermaphrodites were picked from the next generation on these crossing plates and placed onto separate seeded OP50 plates. After egg laying began in these worms, they were picked, anesthetized using levamisole, and observed under confocal microscopy for expression of the desired constructs. Plates that had adults expressing the desired constructs were propagated each generation and then checked by a similar imaging procedure until a homozygous line was established

Live cell imaging
Imaging was performed using an oil immersion objective (Plan Apo 60X/1.4, Nikon) on a laser scanning confocal microscope (Nikon A1) equipped with a CO_2 microscope stage incubator under 5% CO_2 and 37°C. Since EGFP and mTagBFP2 excitation overlaps with iLID activation spectrum, we performed pre-activation imaging as well as deactivation imaging (i.e., condensate disassembly) through mCherry channel only (560 nm excitation), which allowed visualization of only the IDR components. For global activation, cells were imaged sequentially by both mCherry and GFP (488 nm) channels, such that both Core and IDR components were visualized. Most activation protocols were conducted with excitation power of 84 μW/ μm^2 measured with an optical power meter (PM100D, Thorlabs). mTagBFP2 labeled constructs were imaged similarly through 405 nm excitation channel. Global activation protocols were performed with dual channel imaging (568 nm and 488 nm) with optical sectioning of 0.42 μm (pin hole size set to 33.2 μm) and frame intervals of 4.4 s and 2.2 s for 120x120 μm^2 (1024x1024 pix) and 60x60 μm^2 (512x512 pix) frame sizes respectively. In the case where a fast frame rate was desirable (Figures 4A–4C), a frame interval of 0.5 s was used (256x256 pix). For capturing spinodal

decomposition patterns (insets of Figure 4B) optical sectioning was set to a 0.3 µm by minimizing pinhole size. Local activation was performed by activating a pre-defined ROI through stimulation mode at either 488 nm or 405 nm wavelength.

Fluorescence recovery after photobleaching experiments

Fluorescence recovery after photobleaching (FRAP) experiments shown in Figure 1 were performed similarly to local activation protocol while limiting the activation zone to a ~1 µm circle and increasing the photoactivation power by ~100 and 200 fold when photobleaching EGFP labeled cores and mCherry labeled IDR components respectively. Cells were globally activated for few minutes prior to photobleaching in order to acquire steady state in the condensed phases. In order to coordinate between the center of droplets to the predefined photobleaching area, we have pre-nucleated single droplets at regions that were set to be photobleached by performing 1 min of locally activated that preceded the global activation step. Global activation was carried out during fluorescence recovery measurement. Contrary to the near complete photobleaching performed on mCherry labeled IDR, EGFP photobleaching was conducted in relatively weaker power, leading to ~60% photobleaching. The use of weaker power originated from an irreversible response of condensates to high 488 nm power, which resulted in incomplete disassemble after photoactivation was turned off. This incomplete disassembly, which was observed only in droplets that were photobleached with 488 nm at high power (> 1 mW/µm^2), is likely to be related to the iLID module and not to the EGFP and is likely the reason for the incomplete recovery observed in Fluorescence recovery of Cores.

Multi-cycle global activation

Repeated global activation cycles were performed as defined above, with 40 s activation and 72 s deactivation, repeated for a total of 32 times each. The last 16 cycles are shown in Figure 1H as the first 16 cycles allowed sufficient transport of the FUS$_N$ IDR module into the nucleus, leading to continuous increase in valence. After 16 cycles, little change in $\bar{f}$ was observed therefore the last 16 were selected to most reasonably show consistent droplet formation and dissociation kinetics under minimal nuclear transport contribution. We point out that increasing the deactivation time from 72 s to 5 min, such that nuclear IDR levels within the nucleus are fully restored to the pre-activation levels, full reversibility was observed without the need of pre-activation (data not shown). We also note that in the case of non-partitioning IDRs, such as HNRNPA1C that include NLS, full reversibility was observed even when performing rapid on and off cycles.

Multi-cycle local activation with shrinking activation region of interest

Figure 7A shows an experiment in which decreasing fractions of the nucleoplasm is successively exposed to blue light illumination. To prevent changes in activation parameters that would result from using activation regions of interest (ROIs) of different size, the same size ROI is used for each activation cycle. For activations of decreasing fractions, the rectangle is moved down in the y-dimension, so as to only cover 1/2, 1/3, 1/4, and finally 1/6 of the nucleus. Each activation and deactivation step last 140 s and at least 3.5 min respectively.

Western blot for measurements of relative endogenous ferritin and engineered Core expression levels

Untransfected HEK293 cells and those stably expressing FUS$_N$ Corelets were grown to approximately 90% confluency in 60 mm plates. Cells were trypsinized and collected in PBS with protease inhibitor. Cell lysates were prepared by sonication and protein concentration was quantified with Bradford Assay (Millipore Sigma). Samples of 0.4 µg/µL whole cell lysate were prepared in Novex NuPAGE lithium dodecyl sulfate (LDS) buffer (Invitrogen) supplemented with 75 mM dithiothreitol (DTT; Thermo Scientific) as a reducing agent. FTH1 and FTL1 recombinant protein standards (ProSpec) were diluted to 100 ng in 25 µl of the same LDS/DTT buffer. After briefly boiling all samples at 100°C, 25 µl (10 µg protein weight cell lysate, 100 ng protein standard) of denatured sample was loaded to NuPAGE 4%–12% Bis-Tris protein gel and run with NuPAGE MOPS buffer (Invitrogen) at 100 V for 90 min. Wet transfer to a Polyvinylidene difluoride membrane was performed at 30 V for 1 hr in NuPage Transfer buffer (Invitrogen). The membrane was blocked with 5% Non-Fat Dry Milk (Nestle) in TBST. The β-Actin strip was cut from the membrane directly above the 30 kDa and 50 kDa protein standards and probed with rabbit anti-β-Actin (ab8227, abcam) overnight at 4°C. The remaining membrane was probed under the same conditions with mouse anti-FTH1 (MABC602, Millipore Sigma). After washing with TBST, the β-Actin strip was probed with anti-rabbit horseradish peroxidase (HRP) (111-035-144, Jackson ImmunoResearch), and the FTH1-probed membranes were probed with anti-mouse HRP (115-035-062, Jackson ImmunoResearch), both at room temperature for 30 min. Chemiluminescence was induced with SuperSignal West Pico substrate (Thermo) and imaged with a ChemiDoc MP Imaging System (BioRad).

QUANTIFICATION AND STATISTICAL ANALYSIS

Determining diffusion coefficients and absolute concentrations for Corelets components

mCherry fluorescence was converted to absolute concentration using fluorescence correlation spectroscopy (FCS) (Figure S4H). GFP fluorescence conversion was done by determining the exact mCherry-to-GFP fluorescence ratio while using the mCherry fluorescence to concentration ratio as a set point. mCherry-to-GFP fluorescence ratio was determined by equimolar expression of mCherry and GFP monomers in HEK293 cell using the auto-catalytic P2A containing construct mCherry-P2A-EGFP, which unlink the two proteins such that FRET is prevented.

Data for diffusion and concentration of proteins were obtained using with 30 s FCS measurement time. The measurements were performed on HEK293 cells expressing M23 using a laser scanning confocal microscope (Nikon A1) with an oil immersion objective (Plan Apo 60X/1.4, Nikon). All measurements and data analysis were performed using the SymPhoTime Software (PicoQuant).

The autocorrelation function for simple diffusion is:

$$G(\tau) = G(0)\left(1 + \left(\frac{\tau}{\tau_D}\right)\right)^{-1}\left(1 + \left(\frac{\tau}{\kappa^2 \tau_D}\right)\right)^{-0.5}$$

Here, $G(0)$ is the magnitude at short timescales, τ is the lag time, τ_D is the half decay time, and κ is the ratio of axial to radial of measurement volume ($\kappa = \omega_z/\omega_{xy}$). Here, $\omega_{xy} = 0.23$ µm and $\kappa = 3.1$ which is determined by fluorophore dye Atto 550 in water. The parameters τ_D and $G(0)$ are optimized in the fit and are used to determine the diffusion coefficient ($D = \omega_{xy}^2/4\tau_D$) and molecule concentration ($C = (\pi^{3/2}\omega_{xy}^2\omega_z G(0))^{-1}$).(Krichevsky and Gregoire, 2002). Using FCS to measure the Ferritin core and IDR diffusivities in living cells nuclei, we find that $D_{Core} = 3.0+/-0.7$ µm^2/sec and $D_{FUS} = 43.5+/-6.5$ µm^2/sec. Mean and standard deviation of the diffusion coefficient inferred from fitting correlation curves from five individual cells.

Here, the measurement volume is approximated by a three-dimensional Gaussian with two parameters, ω_{xy} and ω_z. However, in living cells, there is a refractive index mismatch that can distort the FCS measurement volume as a non-Gaussian profile. With the refractive index of the cellular nucleoplasm ~1.36 (Choi et al., 2007), this mismatch would lead to an absolute error in diffusion coefficient and concentration of ~20% (Müller et al., 2009). In addition, optical artifacts due to cover slide thickness variation, optical saturation, and aberrations also affect the size of the measurement volume, which lead to errors of 50% (Loman et al., 2008; Petrásek and Schwille, 2008). Therefore, it is difficult to precisely determine molecular concentration and their diffusion coefficient due to unknown actual size of a measurement volume in living cells, an effect which cannot be corrected in a straightforward way. Taking these sources of error into consideration, we estimate our concentration accuracy to be within 2-fold of the actual values.

Image analysis and phase diagram construction

The nucleoplasm boundary (i.e., nucleus subtracted by Core excluding regions such as nucleoli) in each cell before and after photoactivation was determined based on the fluorescence pattern of the partitioning NLS-tagged Core component (EGFP channel) by applying an automated image segmentation MATLAB code. Histograms of fluorescent signal within this segmented region demonstrate single mode distribution of both Core (Figures S4B and S4C) and IDR components in cells prior to activation. Thus, mean EGFP and mCherry fluorescence within these segmented regions could be determined and translated to absolute concentration via the FCS-based concentration estimation mentioned above. To identify dilute and dense phases in photo-activated condensing cells, subsequent segmentation of the nucleoplasm was performed (Figure S4F), based on which area fraction of the two phases was determined (Figure 3E). To accurately determine concentration within the dense and dilute phases, morphological erosion was further performed on the segmented regions associated with the two phases, such that pixels near the interface were excluded from further analysis (Figure S4F) as they misrepresent the expected step function-like interface due to optical resolution limit and partially out-of-focus droplets, which lead to an intensity gradient at the interface. As stated in the text, valence is measured as the ratio of determined IDR and Core concentrations for a particular phase or as the nuclear average. However, individual Cores likely to exhibit some spread in the distribution of IDRs bound to them around the specified mean. This could potentially create a slight shift in the y axis of the phase diagram compared to a system with monodisperse valence. Nevertheless, the observation that similar valency is maintained in the dilute and dense phases (Figure 3D) suggests that the Corelet system does not promote bimodal distribution of valency between phases. While mean nucleoplasmic core concentration is fixed, nucleoplasmic levels of FUS$_N$-based IDR component as well as the mean valence, which is derived from it, continuously increase during activation. This occurs since FUS$_N$-based IDR component (but not in non-partitioning IDR such as HNRNPA1$_C$) have both cytoplasmic and nucleoplasmic subpopulation, where once activation is applied, the fast uptake and sharp depletion of nucleoplasmic IDR component monomers, drives net flow of cytoplasmic IDRs into the nucleus. For that reason, valence values were determined only after steady state is reached (t ~5 min). Contrary to the steady state binodal line, the spinodal line (i.e., the mechanism by which phase separation occurs) was determined accordingly to the valence at t = 0 (see Figure 4).

Fluorescence recovery after photobleaching analysis

FRAP experiments were analyzed by measuring time dependent fluorescence within a circular ROI, ~1 µm in diameter, positioned at the center of the photobleached droplets using imageJ. Error bars represent standard deviation of pixel intensities within the circular ROI.

Determination of Corelet spacing and occupancy in condensates

The maximal concentration of ~25 µM that we have measured in condensates of FUSN-Corelets (Figure 3C) corresponds to density of 1 molecule per 6.66×10^4 nm^3. Assuming for simplicity the local organization follows a cubic lattice configuration, we calculate mean center-to-center inter-particle spacing of 40.5 nm (i.e., between centers of IDR decorated cores). Considering the 12 nm diameter of ferritin and the diameter for the each of the 24 EGFPs, iLIDs, SspBs, and mCherry bound to the core to be roughly 2 nm, we estimate the core diameter to be roughly 25 nm, meaning that the remaining two overlapping FUS$_N$ molecules along the axis between

two cores should occupy the remaining ∼15 nm (i.e., interparticle spacing subtracted by the core size). Similar considerations taking into account the diameters of the components, with a FUS$_N$ diameter taken as 5nm, leads to a volume fraction estimated at 5%.

Simulations

We developed a simple Monte Carlo simulation of the Corelet system, using MATLAB. Simulations were run with 500 "Core" particles, and 1200 "IDR" particles, randomly distributed in a 2D simulation space with reflecting boundary conditions. Particle diffusivity is modeled by introducing a random "kick" at each time step, Δt, such that particles move by an amount (in both x and y) given by $\sqrt{4D_i \varDelta t} \cdot \xi$, where ξ is a normally distributed random variable with mean 0 and standard deviation 1. The particle diffusivity, D_i, was varied for different simulations with most simulations set at the experimentally determined diffusivities, i.e., D_{Core} = 3μm2/sec, D_{IDR} = 43.5μm2/sec. At each time point, the position of each IDR particle is checked to see if it is within a set interaction distance of any Core particle. For particles within a defined activation zone, if the IDR is close enough to bind the Core, and the Core is not already saturated with a defined number of IDRs ("maxidrs"), then the IDR particles bind, by remaining at this fixed position relative to the Core particle position, while the Core particle (and thus associated bound IDR particles) continues with its diffusive motion, updated at each time step. For all simulations, if the diffusive motion of the Core particle takes it outside of the activation zone, then any bound IDR particles are released.
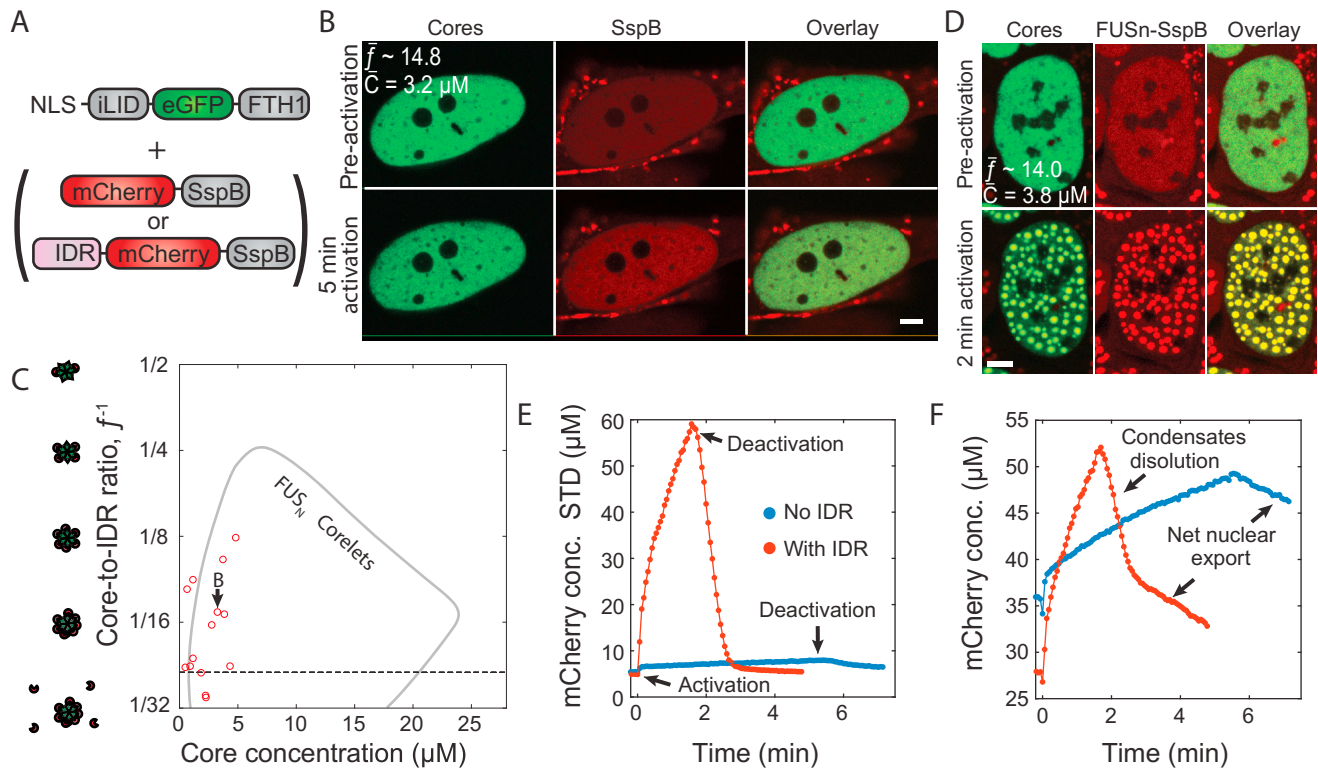
Figure S1. IDR-Free Corelets Do Not Phase Separate, Related to Figure 1

(A) Schematic diagram of Corelet modules with or without IDR fused to mCherry-SspB.

(B) Representative U2OS cell expressing Cores (green) and mCherry-SspB (red) components before and after 5 min photo-activation, showing no puncta formation.

(C) The concentration of cores (3.2 μM) and SspB-to-core ratio (i.e., mean nuclear valence $\bar{f}$, 14.8) position of the cell shown in (B) and other observed IDR-free Corelet expressing cells (red circles) well within the binodal region of FUS_N Corelets (gray boundary), where demixing occurs, as indicated in Figure 3B.

(D) Representative U2OS cell expressing FUS_N Corelets with similar core concentration and f as in (B) undergoing phase separation under similar excitation conditions.

(E and F) Change in standard deviation of mCherry intensity (E) in the nucleus of the cells shown in (B) and (D) during activation showing very little change in IDR-free Corelets compared to FUS_N Corelets. Two transitions are observable in both IDR-containing and IDR-free Corelets that are not related to phase separation. First, upon activation, an instantaneous depletion of SspB-fused components from nuclear regions that exclude cores (compare spatial difference in B during pre-activation, see also Figure S5). Second, a gradual increase in standard deviation and in (F) overall nuclear mCherry intensity followed by a gradual decrease during deactivation due to trafficking of free SspB-fused components across the nuclear membrane (see also Figure S3).
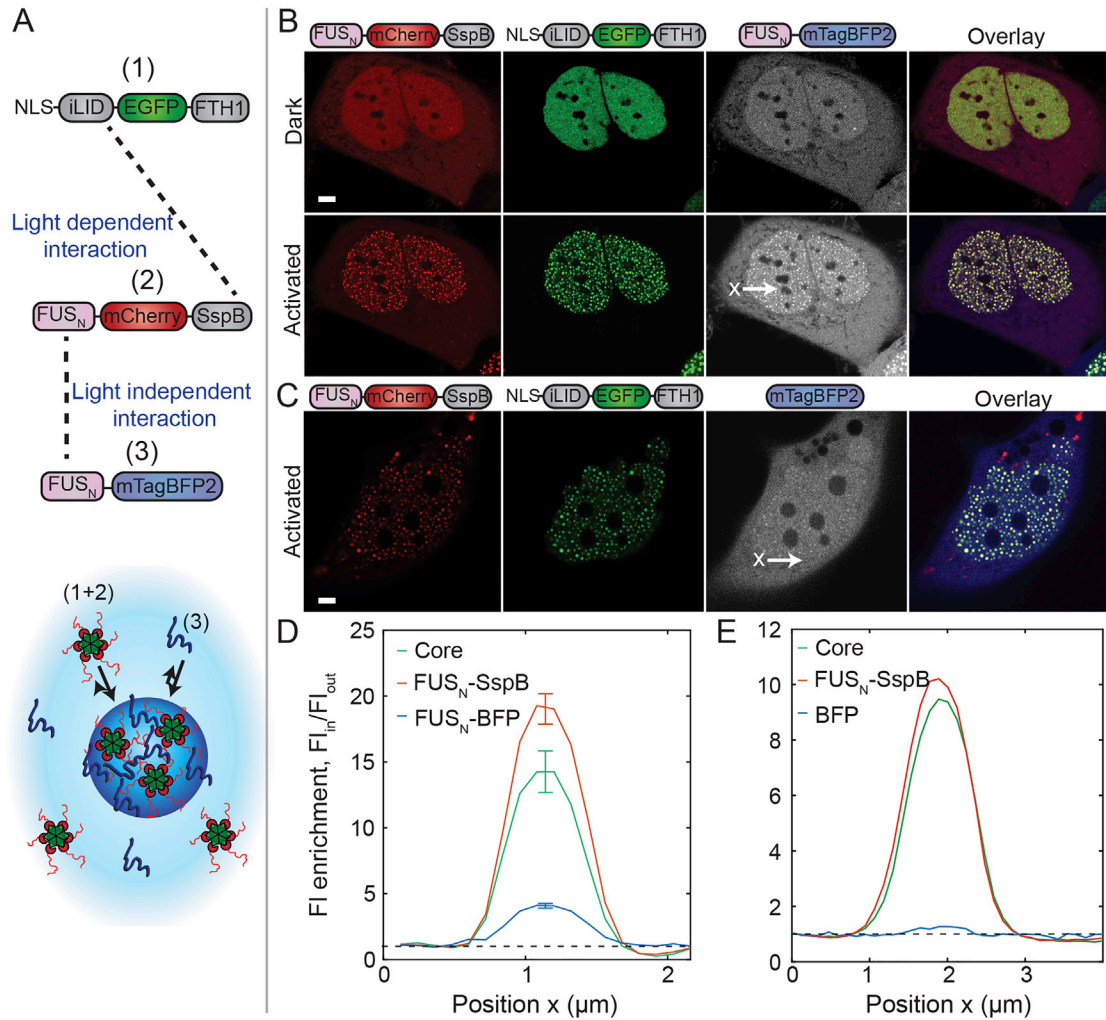
Scale bars are 5 μm.

Figure S2. Recruitment of SspB-Free FUS$_N$ Monomers by FUS$_N$ Corelets, Related to Figure 1

(A) (Top) Schematic diagrams of the two-module Corelet system as well as an SspB-free light-insensitive FUS$_N$ monomer tagged with mTagBFP2. Dotted lines suggest interactions present between the 3 components. (Bottom) Schematic illustration showing recruitment of FUS$_N$ monomers through IDR-IDR interactions.

(B) Fluorescent images of stable HEK293 cells expressing Cores (green), FUS$_N$-SspB (red), and FUS$_N$-mTagBFP2 (gray) before and after 5 min of blue light activation, showing colocalization of all three components.

(C) Fluorescent images of stable U2OS cell expressing Cores (green), FUS$_N$-SspB (red), and FUS$_N$-free mTagBFP2 (gray) showing enhancement of only ∼30% in condensates compared to the dilute phase levels.

(D and E) Quantification of the relative enrichment of the three components inside droplets after 5 min of activation shows fourfold increase in recruited light insensitive FUS$_N$ condensates relative to the dilute phase. (D) is for FUS$_N$-mTagBFP2 and (E) is for mTagBFP2 control. Dashed lines represent unity. Error bars are standard deviation of the mean (n = 5 (D) and n = 1 (E)).
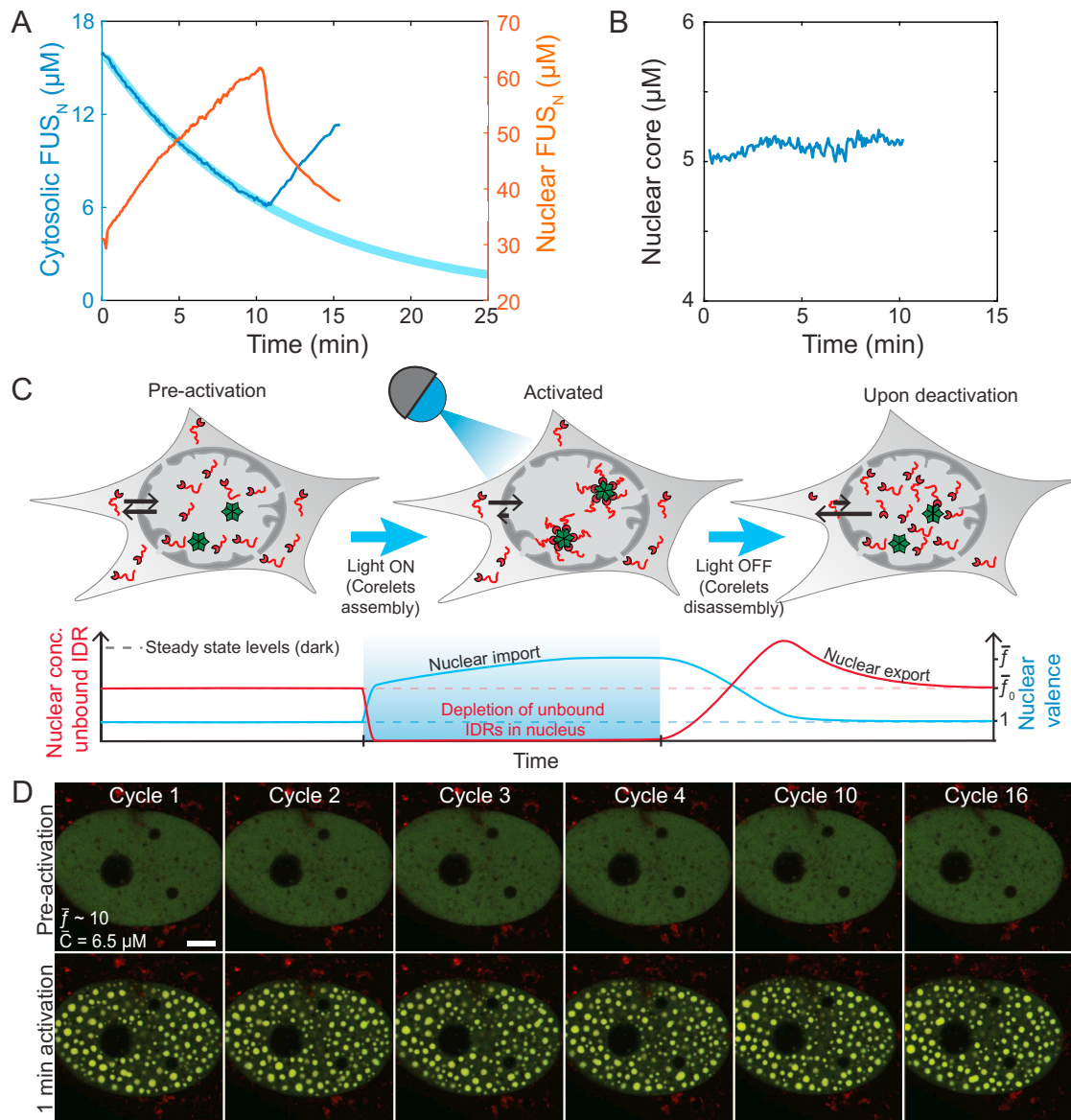
Scale bars are 5 μm.

Figure S3. Transitions in Local Concentration of IDR and Core Components in FUS$_N$ Corelet Expressing U2OS Cells during Activation, Related to Figure 1

(A) FUS$_N$ IDR concentration in nucleoplasm (orange) and cytoplasm (blue) during 10 min activation and 5 min deactivation. In the dark state, NLS-free FUS$_N$ IDR partitions between cytoplasm and nucleoplasm yielding a concentration ratio, $C_{Nuc}/C_{Cyto} \cong 2$. Immediately after activation, the concentration in nucleoplasm begins increasing while the cytoplasmic concentration begins decreasing, suggesting that nucleoplasmic IDR components are quickly captured by cores, leading to a sharp drop in unbound IDRs (monomers) in nucleoplasm, and a net nuclear influx of unbound IDRs from the cytoplasm. The decrease in cytoplasmic concentration is well fit to a simple exponential decay $C_{cy}(t) = C_{cy}(0)exp(-t/\tau)$. This exponential decay toward zero cytoplasmic concentration suggests that nearly the entire nuclear population of IDRs are being captured by the cores and that activated Corelets can be regarded as a single component system, as long as the number of IDR modules do not saturate the potential binding spots on Cores.

(B) Core component concentration in the nucleoplasm does not change significantly during 10 min activation and 5 min deactivation. We also do not observe any sharp drop during the first few seconds of activation, suggesting minimal FRET response between the EGFP of the Core component and the mCherry of the IDR component.

(C) Schematic illustration showing nuclear import and export of unbound IDRs during photoactivation and deactivation. Concentration of unbound IDRs shown in red and mean IDR valence in blue. Note that IDR valence is equal to one without blue light activation as there are no stable IDR oligomers, while it equals the IDR-to-Core ratio during blue light activation, which increases to a steady state with IDR import.

(D) Representative images before and after activation of FUS$_N$ Corelet expressing U2OS cell undergoing multiple activation cycles as shown in Figure 1H. Cell has been pre-activated for 15 min in order to prevent additional changes in valency during activation due to import of cytoplasmic IDR components as shown schematically in (C). We note that pre-activation is not required for demonstrating full reversibility of Corelets driven phase separation with non-partitioning IDRs such as HNRNPA1$_C$ (Figure 2, data not shown). Scale bar is 5 μm.
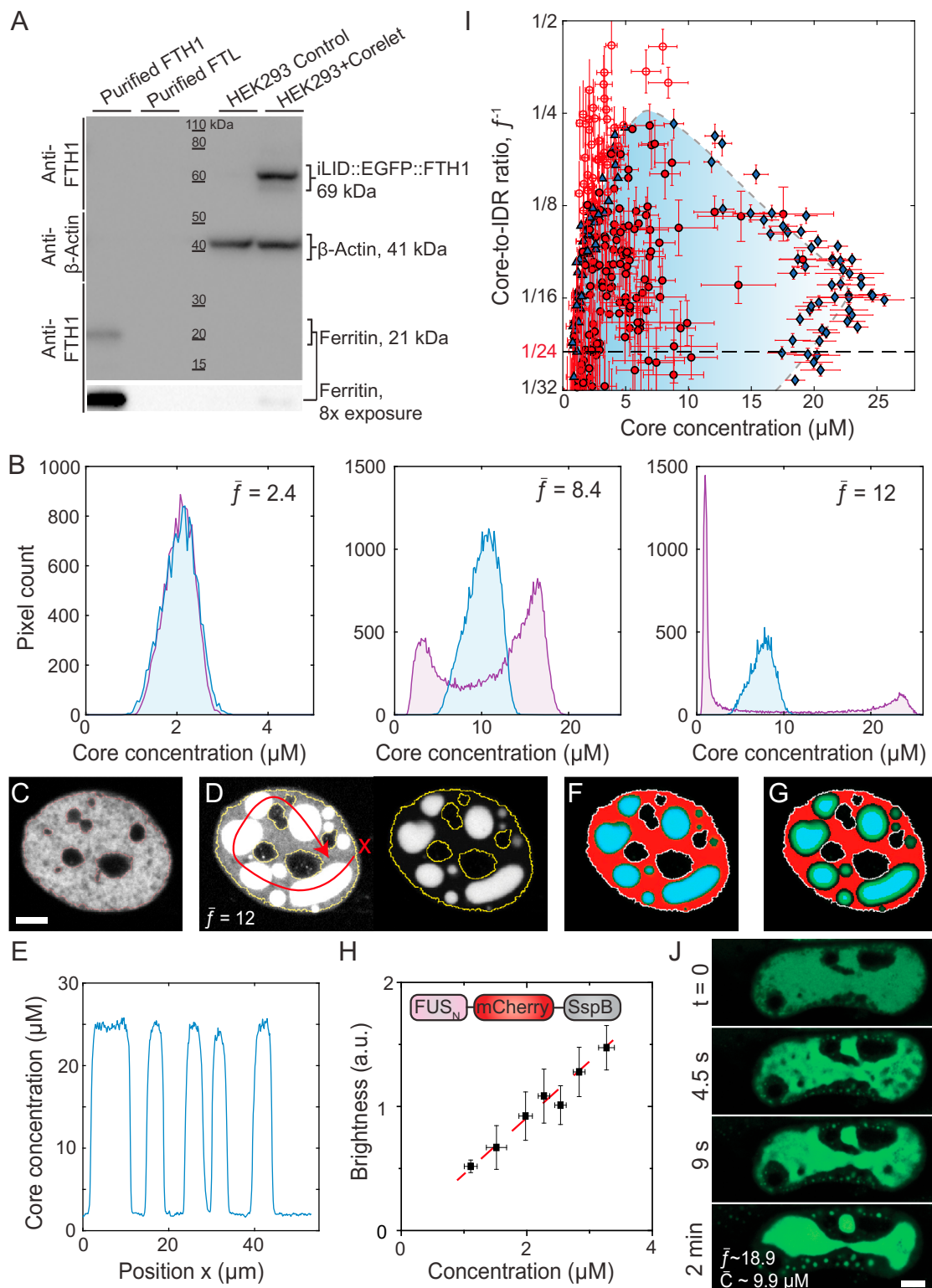
Figure S4. Corelet Phase Diagram Analysis, Related to Figure 3 and STAR Methods

(A) Western blot analysis of ferritin in FUS$_N$ Corelet expressing HEK293 cells (HEK+Corelets) show extremely small amount of native FTH1 as compared to exogenous Core components. This implies that measured valency is not confounded by the presence of endogenous FTH1. Untransfected cells (HEK) act as a negative control. 100 ng of purified heavy chain (FTH1) and light chain (FTL1) ferritin (ProSpec) loaded as positive and negative controls, respectively. Lower panel

(legend continued on next page)

is a replication of marked region imaged with eight times longer exposure. β-Actin shown as an internal loading standard. Calculated molecular weight indicated and band identification is shown to the right, and antibody specificity used for each blot is indicated on the left.

(B) Histograms of Core concentration before (blue) and after (purple) 10-minute photoactivation, for three representative cells with different $[\overline{Core}]$ and $\bar{f}$. Cells with low $\bar{f}$ (left) show no change in response to photo-activation and do not phase separate, while cells with increasing $\bar{f}$ (center and right) yield a greater separation between concentration inside droplets, $[Core]_{Dense}$, and outside droplets, $[Core]_{Dilute}$.

(C–G) Example of image analysis performed for the construction of phase diagrams. (C) Typical FUS$_N$ Corelet expressing cell before and (D) after 10 min of activation presented at low (left) and high (right) intensity contrast, showing (E) uniform fluorescence in dilute and dense phase even in separate droplets (profile along arrow in D). Dilute and dense phase regions were identified by carrying out two successive segmentations, first (D) an intra-nuclear segmentation to identify nucleoplasm, namely nucleus without regions that constitutively exclude Corelet components like nucleoli, and (F) second, an intra-nucleoplasmic segmentation step, to identify area fraction of dilute (red) and dense phases (cyan), as shown and plotted in Figure 3E. (G) The segmented ROIs of dilute (red) and dense phases (cyan) were further morphologically eroded by 8 peripheral pixels (∼1 μm) before mean fluorescence levels were calculated.

(H) FUS$_N$-mCherry-SspB fluorescence to concentration calibration curve measured in cellular nucleoplasm using fluorescence correlation spectroscopy. Error bars are standard deviation of the mean with n = 10.

(I) Phase diagram of FUS$_N$ Corelets as shown in Figure 3 including error bars for the standard deviation for all segmented ROIs. While mean cellular values (red circles) represent post-activation values modified by cytoplasm-to-nucleoplasm transported IDRs, the corresponding error bars represent the monomodal pre-activation distribution (e.g blue histograms in (B)).

(J) Representative cell with very high Core and FUS$_N$ IDR concentration undergoing phase separation even in the dark state. Pre-activation phase separated cells still respond to photo-activation, leading to decrease in dilute phase concentration and increase in dense phase concentration with concentration that follows the binodal line.

Scale bars are 5 μm.

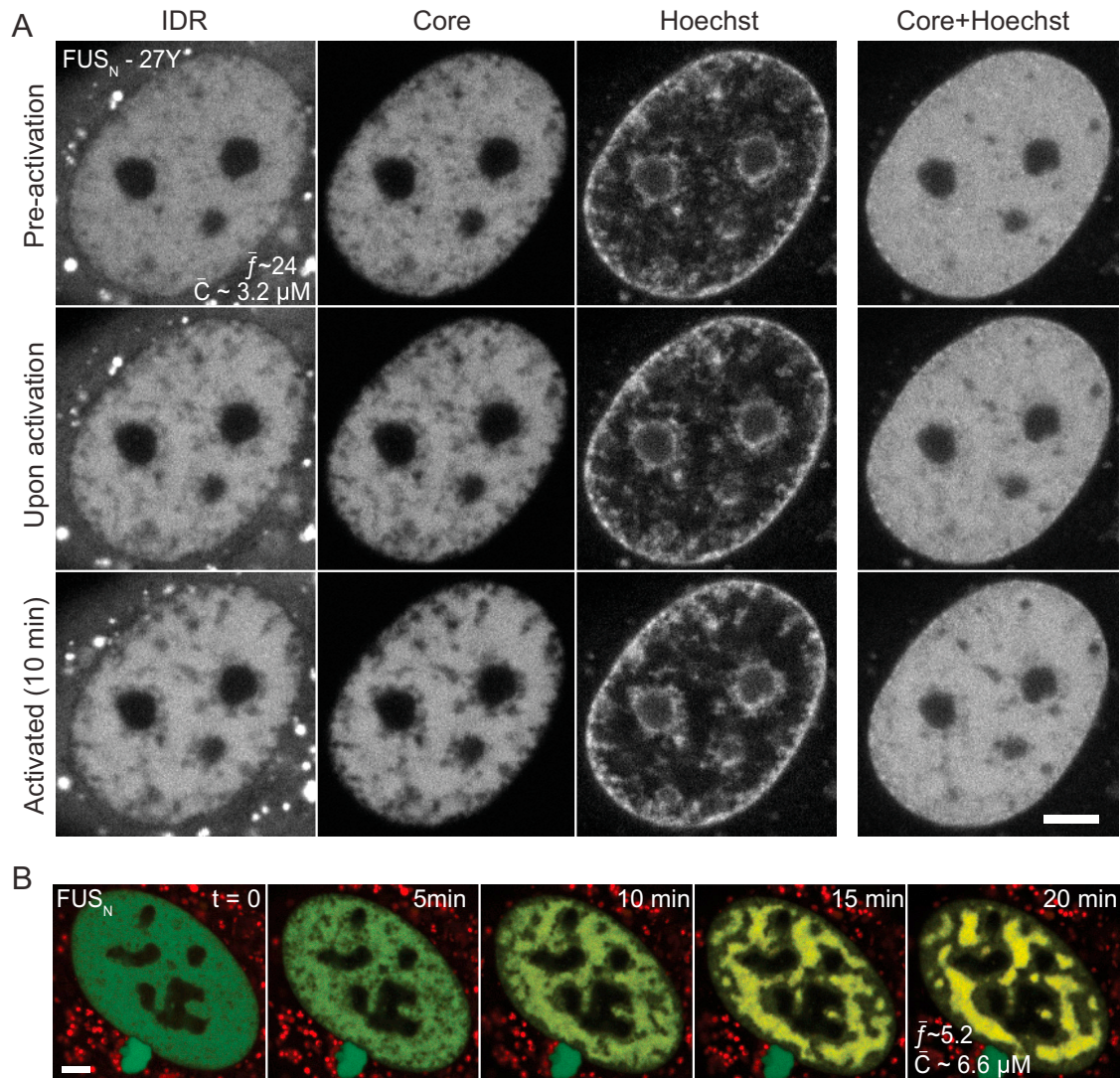**Figure S5. Nonactivatable Cells Still Show Light-Induced Corelet Patterning as a Result of Chromatin Exclusion, Related to Figure 5**

(A) FUS_N-27Y Corelets in U2OS cells before activation (top), during the first frame of activation (middle), and following 10 min blue light illumination (bottom). For each, IDR and Core module as well as Hoechst dye signals are shown in grayscale. To the right, the combined Core and Hoechst signal is shown, both in grayscale. This Corelets construct fails to show distinct phase separation, but a patterning of the localization of the two Corelets modules are still observed upon blue light activation, which occurs most prominently for high valency cores, as in this example ($\bar{f} = 24$). Notably, the regions of Corelet module exclusion during activation are complemented by regions of strong Hoeschst signal (see combine Core+Hoechst signal, right).

(B) Light-induced patterning is similarly observed in FUS_N Corelets in U2OS cells; Cores, Green; IDR, Red. A cell initially with $\bar{f} \sim 3$ is unable to initially phase separate but forms patterns, presumably excluded from chromatin. With extended blue-light illumination, IDR is transported into the nucleus, increasing $\bar{f}$ to 5.2, allowing for phase separation after 20 min, as evidenced by increased enrichment. Scale bars are 5 μm.